Practical realization of chiral nonlinearity for strong topological protection

Xinxin GUO[1], Lucien Jezequel[2], Mathieu Padlewski[1], Hervé Lissek[1], Pierre Delplace[2] and Romain Fleury[3⋆]

1 École Polytechnique Fédérale de Lausanne, Signal Processing Laboratory LTS2, CH-1015 Lausanne, Switzerland.
2 École Normale Supérieure de Lyon, CNRS, Laboratoire de physique, F-69342 Lyon, France.
3 École Polytechnique Fédérale de Lausanne, Laboratory of Wave Engineering, CH-1015 Lausanne, Switzerland.
⋆ romain.fleury@epfl.ch

Abstract

Nonlinear topology has been much less inquired compared to its linear counterpart. Existing advances have focused on nonlinearities of limited magnitudes and fairly homogeneous types. As such, the realizations have rarely been concerned with the requirements for nonlinearity. Here we explore nonlinear topological protection by determining nonlinear rules and demonstrate their relevance in real-world experiments. We take advantage of chiral symmetry and identify the condition for its continuation in general nonlinear environments. Applying it to one-dimensional topological lattices, we can obtain definite evolution paths of zero-energy edge states that preserve topologically nontrivial phases regardless of the specifics of the chiral nonlinearities. Based on an acoustic prototype design, we theoretically, numerically, and experimentally showcase the nonlinear topological edge states that persist in all nonlinear degrees and directions without any frequency shift. Our findings unveil a broad family of nonlinearities compatible with topological non-triviality, establishing a solid ground for future drilling in the emergent field of nonlinear topology.

Publication information to appear upon publication.

Received Date
Accepted Date
Published Date

Contents

---

1 Introduction

Topological protection has received a surge of interest owing to its strong immunity to parametric perturbations and geometrical defects. It has been investigated on versatile platforms, from quantum mechanics [1] to multifarious classical realms such as electronics [2–5], photonics [6–10] and phononics [11–20]. In contrast to the tremendous attention paid to linear physics and band theory, topological research has less accented on the intersections with nonlinear dynamics [10, 21, 22], despite the ubiquity of nonlinearity in nature. The nonlinear sources exploited for topological purposes include varactor diodes inserted in electrical circuits [4, 5, 23–25], optical materials with intensity-dependent refractive index [10, 26–28], geometry [29, 30] or nonlinear stiffness [31–33] of mechanical structures, and active means that create nonlinearity together with non-Hermiticity [34]. However, the types of nonlinearities are rather homogeneous in previous surveys, with a strong dominance of Kerr-like onsite nonlinearities [5, 6, 10, 23, 26, 27, 31, 33, 35–42], due to their ease in passive realizations and the link to bosonic quantum systems through the well-known Gross-Pitaevskii equation [43]. Exceptions arise mainly from the use of specific lasers [28, 34] or electrical elements [4, 25], whose self-focusing or defocusing behaviors are described by saturable nonlinear gains.

The nonlinear effects, once triggered, have resulted in topologically nontrivial phases that were mostly trivial in the linear regime [10, 22], allowing for many fascinating phenomena such as first- or second-order topological insulators [5, 26, 32, 39], soliton propagation [27–29, 31, 37, 44, 45], and higher harmonic generations [24, 46–48]. Nevertheless, studies reported to date possess their own specific effective range of nonlinearities. Some of them have been restricted to weak nonlinear magnitudes to approach theoretical models and/or to enable theoretical analyses (viable linearization and perturbation methods) [4, 5, 31, 35, 40, 46]. Others, on the other hand, have required nonlinearity strong enough to activate nonlinear states (e.g., solitons) or to localize them clearly (e.g. corner topological states). A few have explored large intervals of nonlinear levels from low to high (before chaos), but with the edge modes/states shifted in frequency [23, 33, 36, 38, 49], ultimately destroying topological phases due to nonlinearity-induced symmetry breaking. Nonlinear topology, discovered within limited contents and extents of nonlinearity, has hardly been discussed from a fundamental nonlinear perspective thus far. That is, taking the stand on topological demands, what nonlinearities are actually needed? Is it feasible in practice to keep topological attributes intact across all nonlinear magnitudes?

To tackle the question, here we unlock limitations to the manipulation of nonlinear topological systems in theory and practice, by satisfying a symmetry that maintains topological non-triviality permanently. Different types of symmetries can enable topological phases of matter [6, 12, 50], including time-reversal symmetry [50], reflection symmetry [51], Parity-Time symmetry [34], chiral symmetry [52, 53] or derived sub-symmetries [54]. Our study utilizes chiral symmetry that is closely related to the emergence of zero-energy topological edge states [55]. We first identify the nonlinear condition for symmetry preservation in general periodic systems. We then introduce eligible nonlinearities in one-dimensional (1D) lattices to alter the linearly produced stationary topological edge states. Their variations are qualitatively predictable assuming chiral nonlinearities with general monotonic dependence on amplitudes. A concrete nonlinear case is finally examined in a theoretical lumped element circuit and in the equivalent real active nonlinear acoustic system. We confirm theoretically, numerically, and experimentally that under chiral symmetry, nonlinear edge states can sustain their topologically nontrivial phases while never shifting in frequency.

2 Chiral symmetry for general nonlinear periodic systems

In terms of the Hamiltonian $\mathbf{H}$ of the system, and in the presence of arbitrary nonlinearities and non-localities depending on the different degrees of freedom $(\mathrm{a}_i, \mathrm{b}_j, \mathrm{c}_k, \cdots)$ contained in the system, chiral symmetry implies that $\Gamma\mathbf{H}(\mathrm{a}_i, \mathrm{b}_j, \mathrm{c}_k, \cdots)\Gamma^\dagger = -\mathbf{H}(\mathrm{a}_i, \mathrm{b}_j, \mathrm{c}_k, \cdots)$, with Γ the chiral operator and $\dagger$ the conjugate transpose [53]. In the chiral base of the degrees of freedom, where $\Gamma = \begin{bmatrix} 1_\mathrm{a} & 0 \\ 0 & -1_\mathrm{b} \end{bmatrix}$ with 1_a and 1_b the identity matrices of random sizes, this definition is equivalent to say that $\mathbf{H}(\mathrm{a}_i, \mathrm{b}_j, \mathrm{c}_k, \cdots)$ is block off-diagonal, namely

$$\mathbf{H}(\mathrm{a}_i, \mathrm{b}_j, \mathrm{c}_k, \cdots) = \begin{bmatrix} 0 & \mathrm{h}(\mathrm{a}_i, \mathrm{b}_j, \mathrm{c}_k, \cdots) \\ \mathrm{h}^\dagger(\mathrm{a}_i, \mathrm{b}_j, \mathrm{c}_k, \cdots) & 0 \end{bmatrix}. \tag{1}$$

Notably, there are no specific restrictions on the nonlinearities in $\mathrm{h}(\mathrm{a}_i, \mathrm{b}_j, \mathrm{c}_k, \cdots)$ in Eq. (1). They can, in principle, take any form, and rely randomly on the system elements, even in a non-local way. The only requirement is that the sites of the same chirality must be uncoupled from each other. Conversely, any nonlinearity that creates couplings among them will inevitably cause symmetry breaking, as is the case with the extensively inquired Kerr-like onsite nonlinearity [5, 6, 10, 23, 26, 27, 33, 35–42].

3 Generalized nonlinear topological protection with chiral symmetry

The satisfaction of Eq. (1) allows for chiral symmetry in Hamiltonians of any dimension. For a direct application, we focus on the zero-energy edge states in 1D dimerized lattices, where Eq. (1) is already met by the 2x2 Hamiltonian in the natural base. We start with the linear chiral case, for which, the recurrent relations read: $\eta_\mathrm{L}\mathrm{a}_n + \mathrm{a}_{n+1} = 0$ and $\eta_\mathrm{L}\mathrm{b}_n + \mathrm{b}_{n-1} = 0$, where a_n and b_n are the amplitudes of the two sites of the n-th unit cell, and the N sites a_n (b_n) constitute the entire sublattice A (B) of the system. A topologically nontrivial phase is obtained if the hopping ratio η_L (ratio between the hopping terms) is smaller than one. The resulting linear topological edge state is displayed in Fig. 1, where the sites a_n carry a decrease in amplitudes along A, with the descent rate fixed by η_L. The presence of chiral symmetry makes the sites b_n stay stationary, independent of a_n.

When nonlinearities get involved in a way that respects Eq. (1), the system energy relations read:

$$0 = a_{n+1} + \left[\eta_L + \eta_{NLa}(a_{n+i}, b_{n+j})\right] a_n, \qquad 0 = b_{n-1} + \left[\eta_L + \eta_{NLb}(a_{n+k}, b_{n+l})\right] b_n, \qquad (2)$$

This suggests that, under chiral symmetry, the participation of nonlinearity results only in modifications in the hopping ratios. They are transformed from the linear invariant η_L to the amplitude-dependent nonlinear variables $\eta_L + \eta_{NLa}(a_{n+i}, b_{n+j})$ applied to a_n and $\eta_L + \eta_{NLb}(a_{n+k}, b_{n+l})$ applied to b_n. a_{n+i} and b_{n+j} (a_{n+k} and b_{n+l}) refer to each site that the nonlinearity in η_{NLa} (η_{NLb}) depends on. They can be arbitrary in the system, i.e., the integer i or j or k or l can be zero if the dependency occurs within the n-th unit cell, or nonzero if the dependency is on the other interacting unit cells.

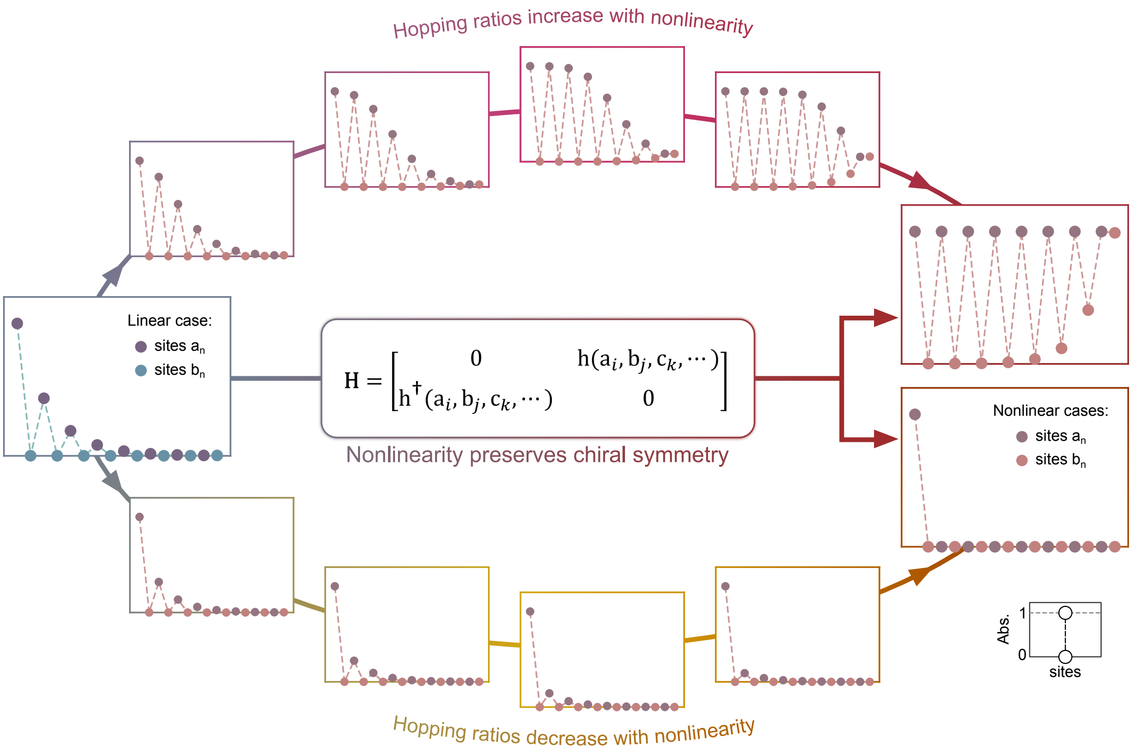

Figure 1: **Qualitative estimations of the evolution laws for zero-energy edge states in 1D dimerized systems with symmetry-preserving nonlinearities.** Profiles of the zero-energy edge state that is initially (linearly) topological and then varied as chiral nonlinearities increase and decrease the hopping ratios on sublattice A, respectively. In each profile, the amplitude of the first site a_1 is fixed at 1. The requirement on the Hamiltonian **H** is explained in Eq. (1). The variation trends apply to the entire class of nonlinearities that lead to monotonic changes in the hopping ratios as the site amplitudes increase.

Unlike a previous theoretical study discussing one particular form of nonlinearity [53], here we predict edge state variations under generalized chiral nonlinearities and validate them experimentally. We consider the most common relationship between site amplitude and nonlinear effects, namely nonlinearities cause monotonic changes in the hopping ratios with increasing site amplitudes. A broad range of classical nonlinearities satisfy this condition, from polynomial laws (quadratic or cubic, etc.) to saturable effects. In addition, non-linear laws are not restricted to local effects. We first deal with nonlinearities that are positively correlated with amplitudes. Based on $a_n > a_{n+1}$ of the linear state, these nonlinearities lead to $|\eta_{\mathrm{NLa}}(a_{n+i}, b_{n+j})| > |\eta_{\mathrm{NLa}}(a_{n+1+i}, b_{n+1+j})|$ in the early nonlinear stage (negligible effects of sites in B, since they carry zero amplitude initially), where the sign of η_{NLa} determines whether nonlinearity increases or decreases the hopping ratios on A. If $\eta_{\mathrm{NLa}} < 0$, we have $\eta_{\mathrm{L}} + \eta_{\mathrm{NLa}}(a_{n+i}, b_{n+j}) < \eta_{\mathrm{L}} + \eta_{\mathrm{NLa}}(a_{n+1+i}, b_{n+1+j}) < \eta_{\mathrm{L}} < 1$, i.e., the hopping ratios are diminished by nonlinearity, with the decrement less and less along A. As nonlinearity is further strengthened, its positive dependence on amplitudes perpetuates the above law. The first hopping ratio remains thus the smallest, always yielding the largest reduction of amplitude from a_1 to a_2. Following this trend, we reach a limit situation where solely the first site a_1 has a nonzero amplitude. The sites b_n in B remain at zero amplitude, owing to chiral symmetry and the fast decay of the nonlinear mode that prevents it from reaching the other end of the system. The total expected edge state variations for nonlinearity decreasing the hopping ratios on A ($\eta_{\mathrm{NLa}} < 0$) are depicted graphically in the lower branch in Fig. 1.

The reasoning applies likewise to the opposite scenario of $\eta_{\mathrm{NLa}} > 0$, where $|\eta_{\mathrm{NLa}}(a_{n+i}, b_{n+j})| > |\eta_{\mathrm{NLa}}(a_{n+1+i}, b_{n+1+j})|$ results in $\eta_{\mathrm{L}} + \eta_{\mathrm{NLa}}(a_{n+i}, b_{n+j}) > \eta_{\mathrm{L}} + \eta_{\mathrm{NLa}}(a_{n+1+i}, b_{n+1+j}) > \eta_{\mathrm{L}}$. Namely the hopping ratios are increased by nonlinearity, with the increment smaller and smaller along A. Remarkably, the first ratio is the largest here, contrary to the previous case of $\eta_{\mathrm{NLa}} < 0$. The enhancement of nonlinearity impels it to first attain 1, at which moment the site a_2 acquires the same amplitude as a_1. After that, if nonlinearity still can increase the hopping ratio, a_2 exceeds a_1 in amplitude. The continuation along this direction makes the ascent of a_2 incessant and towards an infinite level, inevitably ending with the system instability. For this reason, to allow stable states at all nonlinear magnitudes, the nonlinearity should always keep the first hopping ratio at 1 once $a_2 = a_1$ is reached. The other hopping ratios follow the same result due to the periodicity of the system. That is, for $\eta_{\mathrm{L}} + \eta_{\mathrm{NLa}}(a_{n+i}, b_{n+j})$ applied to a_n, we have $\eta_{\mathrm{L}} + \eta_{\mathrm{NLa}}(a_{n+i}, b_{n+j}) = 1$ once $a_{n+1} = a_n$. Such a relationship easily holds if the nonlinear hopping terms for a_n and a_{n+1} are dominated by their site amplitudes, respectively, as exemplified by the explicit case in Fig. 2a (see Eqs. (A.5) and (A.6)). It shows that, as the nonlinearity strengthens, the sites a_n ($n \geq 2$) successively arrive at the amplitude of a_1 and then sustain there. Ultimately, they will exhibit the same amplitude, forming a 'plateau' in A.

For actual systems with finite dimensions, the zero-energy mode reaches the other edge of the system when all sites in A are nonlinearly endowed with nonzero amplitudes. In this case, the excited opposite zero mode causes the amplitude of the sites in B to begin to rise, with a lowering from b_n to b_{n-1}, i.e., a heightening along the structure. No conclusion can be drawn about the direction of changes in the hopping ratios on B. Their increase or decrease are separate from those on A, as Eq. (1) states. Despite this, it is certain that from an initial value of less than 1, the nonlinearity should drive the hopping ratios up to 1 at most, as we discovered earlier through the sublattice A. The extreme nonlinear result can hereby be extrapolated: sites b_n conduct an increase in amplitude along B, with merely the first b_1 at rest. Our overall estimates for the case of nonlinearity increasing the hopping ratios on A ($\eta_{\mathrm{NLa}} > 0$) are delineated schematically in the upper branch in Fig. 1, where the pattern in B results from the explicit nonlinearity considered later in Fig. 2a.

Performing the same analysis as above for nonlinearities that are negatively correlated with site amplitudes, one will obtain the same evolution limits as in Fig. 1. Collectively, accounting for a monotonic amplitude dependence of the chiral nonlinearity, the hopping ratios can always stay smaller than or at most equal to 1 for both sublattices A and B. Therefore, the derived variation tendencies lead to the nonlinear edge states that remain topologically nontrivial, whatever the nonlinear contents. A result similar to part of Fig. 1 was previously observed in a numerical attempt [31], but with a particular nonlinear management and without discussing the underlying symmetry cause. Distinctively, here our starting point is to interrogate chiral symmetry, thus unveiling the entire class of nonlinearities that ensures topological non-triviality.

4 Example of nonlinear topological protection with chiral symmetry

To confirm our anticipations in Fig. 1, we take the example of a concrete finite system represented by the lumped element circuit in Fig. 2a. It consists of 8 unit cells, each with linear and nonlinear resonators. The linear resonators LF_{2k-1} and LF_{2k} are identical and exhibit a resonance at a lower frequency f_{LF}. The nonlinear resonators HF_{2k-1} and HF_{2k} resonate at the same frequency f_{HF}, higher than f_{LF}, while a larger (linear) resonance bandwidth is assigned to HF_{2k-1} compared to HF_{2k}. The generators $V^{(NL)}_{2k-1}$ ($V^{(NL)}_{2k}$) introduce nonlinearity into HF_{2k-1} (HF_{2k}), with the explicit nonlinear laws given also in Fig. 2a. The overall system allows stationary topological edge states at two different frequencies (Appendix A.1, Fig. 4), dominated by the resonance of LF_n and HF_n ($n = 2k-1$ and $2k$), respectively. The voltages carried by LF_{2k-1} (LF_{2k}) correspond to the amplitudes of sites a_n (b_n). In the linear regime, the hopping terms for a_n (b_n) and a_{n+1} (b_{n-1}) are directly mapped to the capacitances $C^{(HF)}_{2k-1}$ in HF_{2k-1} and $C^{(HF)}_{2k}$ in HF_{2k}. In the nonlinear regime, instead, they are dictated by the nonlinearity engaged. Their amplitude dependence is complex: it is not only on the sites a_n and b_n inside the associated n-th unit cell, but also on the sites b_{n-1} and a_{n+1} in the adjacent ones (Eqs. (A.5) and (A.6)). Despite this complexity, the chosen nonlinearities are rigorously chiral.

Our attention is devoted to the topological edge state where the resonance of HF_n prevails. Its nonlinear evolution is revealed in Fig. 2b. In the initial linear scenario, the hopping ratio is defined at around 0.41 (equal to $C^{(HF)}_{2k}/C^{(HF)}_{2k-1}$). The edge state frequency f_H is recognized from the site spectra in Fig. 2b, at the zero amplitudes of all sites b_n. Nonlinearity is then triggered and prescribed using the constant parameter G_{NL} in the nonlinear law. When G_{NL} is decreased along negative values, the hopping ratios on sublattice A are gradually enlarged. The first ratio keeps receiving the greatest increment. It takes the lead to reach 1, followed by the others in succession. At the very end, the plateau on A is infinitely approached, with solely the last hopping ratio still small. Conversely, in the direction $G_{NL} > 0$, nonlinearity incessantly reduces the hopping ratios on A. The relative descent (with respect to the former site) of a_2 remains the largest compared to the other sites. The extreme case of only a_1 surviving is also attained. As for the sites b_n in B, their amplitudes rise exclusively after the activation of the opposite zero mode (along $G_{NL} < 0$), presenting the expected increasing order from b_1 to b_8.

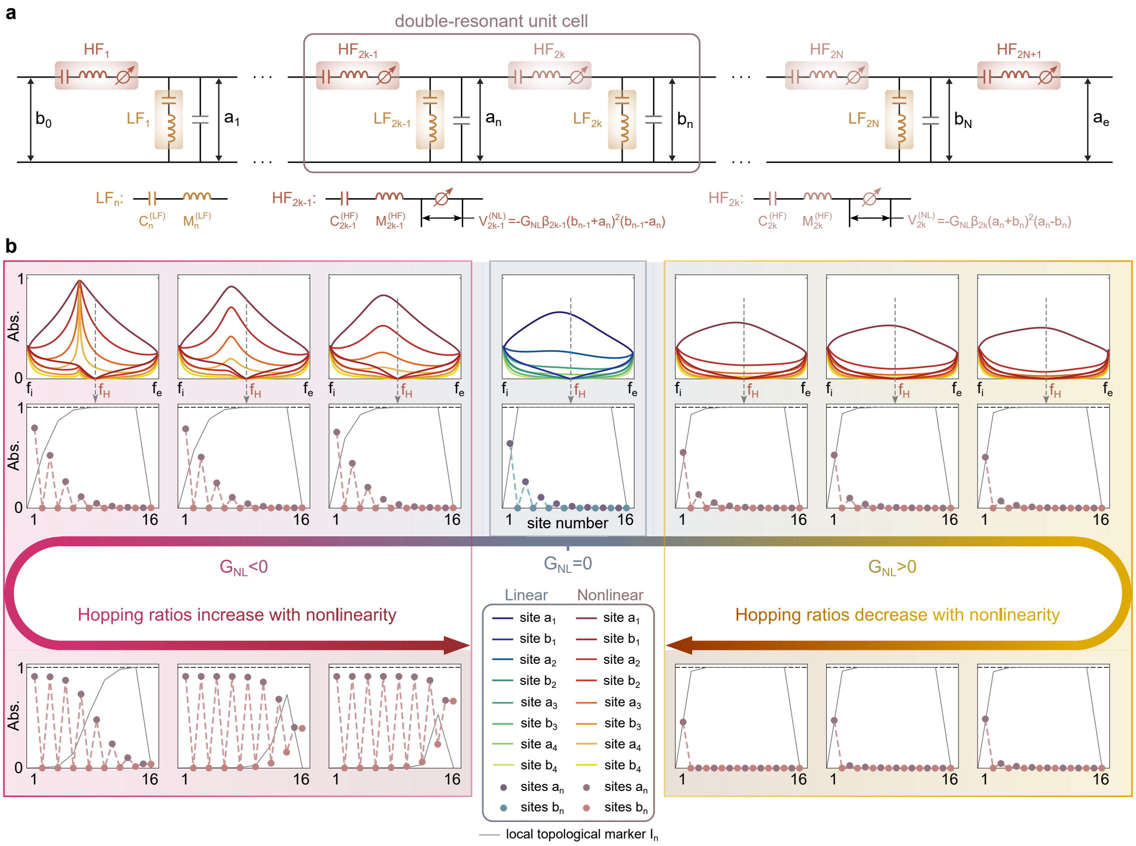

Figure 2: **Evolution of the chiral symmetry protected nonlinear topological edge states: theoretical demonstration in a lumped element circuit with coupled resonators.** (**a**) The considered 1D nonlinear system. It is made of 8 unit cells, each composed of 2 linear resonators LF_n and 2 nonlinear resonators HF_n ($n = 2k-1$ and $2k$) where nonlinearity is added through the generators $\mathrm{V}_n^{(\mathrm{NL})}$. (**b**) Nonlinear variations of the linearly generated stationary topological edge state, under the intervention of the nonlinearity given in (**a**). The nonlinear levels and directions are tuned by the constant parameter G_{NL} in the nonlinear law. It increases (decreases) the hopping ratios on sublattice A with $\mathrm{G}_{\mathrm{NL}} < 0$ ($\mathrm{G}_{\mathrm{NL}} > 0$). The edge state frequency f_{H} is identified from the spectra of a_n and b_n ($\mathrm{n} = 1, 2, 3, 4$) in the frequency range of $[\mathrm{f}_{\mathrm{i}},\mathrm{f}_{\mathrm{e}}]$. All the edge state amplitudes in (**b**) are normalized to the same value. They are obtained with the Harmonic Balance Method (Appendix A.3), and the results for more cases are summarized in Fig. 6. A time domain analysis with the time-integration method is outlined in Appendix B.1 (Fig. 7). In addition to the edge states, the local topological marker [53] $\mathcal{I}_n$ (of the n-th unit cell, drawn at the location of each b_n) is equally displayed for each case (gray lines), which takes values between 0 (not topological) and 1 (topological, indicated by dashed lines).

To reveal the topological aspect of the system, we plot for each unit cell n, the local topological marker $\mathcal{I}_n$ (Fig. 2b) that generalises in real space and for finite size systems, the bulk winding number of 1D chiral symmetric insulators [53]. This marker applies to the linearisation of Eq. (2) around a given nonlinear mode and captures the topology of small perturbations around it. It is particularly suitable for systems with inhomogeneous hopping amplitudes, such as ours, where the lattice translation invariance breaks down and the usual bulk winding number, defined in the Brillouin zone, becomes inappropriate. At an interface between a topological region where $\mathcal{I}_n = 1$ and a topologically trivial region where $\mathcal{I}_n = 0$, the linearised system also develops a zero-energy mode. Due to chiral symmetry, smoothly increasing the amplitude of the nonlinear edge state amounts to adding this linearized zero-mode to the nonlinear background zero-mode without changing its frequency [53]. Therefore, high-amplitude nonlinear modes can be obtained by summing up linearized chiral-symmetry-protected topological zero modes captured by $\mathcal{I}_n$. When nonlinear magnitude is increased along $\mathrm{G_{NL}} > 0$, the interface between the topological phase where $\mathcal{I}_n = 1$ and the edge where $\mathcal{I}_n$ vanishes becomes sharper. The nonlinear edge mode is thus localized more and more on a single site at the edge. In contrast, when $\mathrm{G_{NL}} < 0$, the high amplitude region is associated with a vanishing topological marker, indicating a trivial phase, while low amplitude regions are still topological. The interface zero mode is displaced toward the bulk with increasing nonlinear magnitude along $\mathrm{G_{NL}} < 0$. Accordingly, the amplitude rise of the nonlinear mode also shifts toward the bulk, which further displaces the topological transition between $\mathcal{I}_n = 1$ and $\mathcal{I}_n = 0$ in a self-sustaining loop, leading to a plateau shape of the nonlinear edge state in the end.

We confirm with Fig. 2b that in our system, the chiral nonlinearities maintain the topological edge state at its linearly produced frequency $\mathrm{f_H}$. Contrarily, if nonlinearity breaks the symmetry, the edge state loses its topological features: its amplitude rises on both sublattices A and B, and its frequency shifts away from $\mathrm{f_H}$ (see Figs. 8, 10 and 14 in Appendix B). The site spectra in Fig. 2b evidence in addition that the amplitude relation of $\mathrm{a}_{n+1} < \mathrm{a}_n$ is linearly valid over the entire frequency range of $[\mathrm{f_i}, \mathrm{f_e}]$ displayed therein. It can be nonlinearly transformed up to $\mathrm{a}_{n+1} = \mathrm{a}_n$ only, as the state at $\mathrm{f_H}$ shows. Not surprisingly, if nonlinearity is further enhanced from an already reached $\mathrm{a}_{n+1} = \mathrm{a}_n$, instability would occur at the related frequency. The leftmost spectra in Fig. 2b corresponds to the stability limit of this situation, where the site a_1 is caught up by a_2 at a frequency different from $\mathrm{f_H}$. However, the nonlinear edge state at $\mathrm{f_H}$ is perpetually stable, since its variations always satisfy $\mathrm{a}_{n+1} \leq \mathrm{a}_n$. Collectively, the nonlinear results in Fig. 2b fully demonstrate our inferences for the general context of nonlinearity.

5 Experimental validations

After exploration of the theoretical lattice (Fig. 2), an equivalent active nonlinear acoustic system is adopted for experimental validation (Fig. 3a). A waveguide is used for connecting all the elements. Passive Helmholtz resonators are mounted on its (top) side to play the role of the linear LF_n, while electrodynamic loudspeakers are inserted inside and are actively controlled to act as the nonlinear HF_n. The control for each loudspeaker involves a feedback loop, where a nonlinear control law is appropriately defined based on the acoustic pressures measured on both faces of the loudspeaker membrane (Appendix A.6 and Fig. 11). The control output is returned to the loudspeaker terminals in real-time in the form of a drive current, achieving active resonators HF_n with fully adjustable and reconfigurable characteristics. A total of 8 unit cells are constructed in experiments, each composed of two equally spaced Helmholtz resonators and two equally spaced active loudspeakers. The sub-wavelength portions of tube $\mathrm{V_a}$, enclosed by adjacent speakers, behave similarly to capacitors. Accordingly, the system in Fig. 3a realizes the theoretical lattice in Fig. 2a.

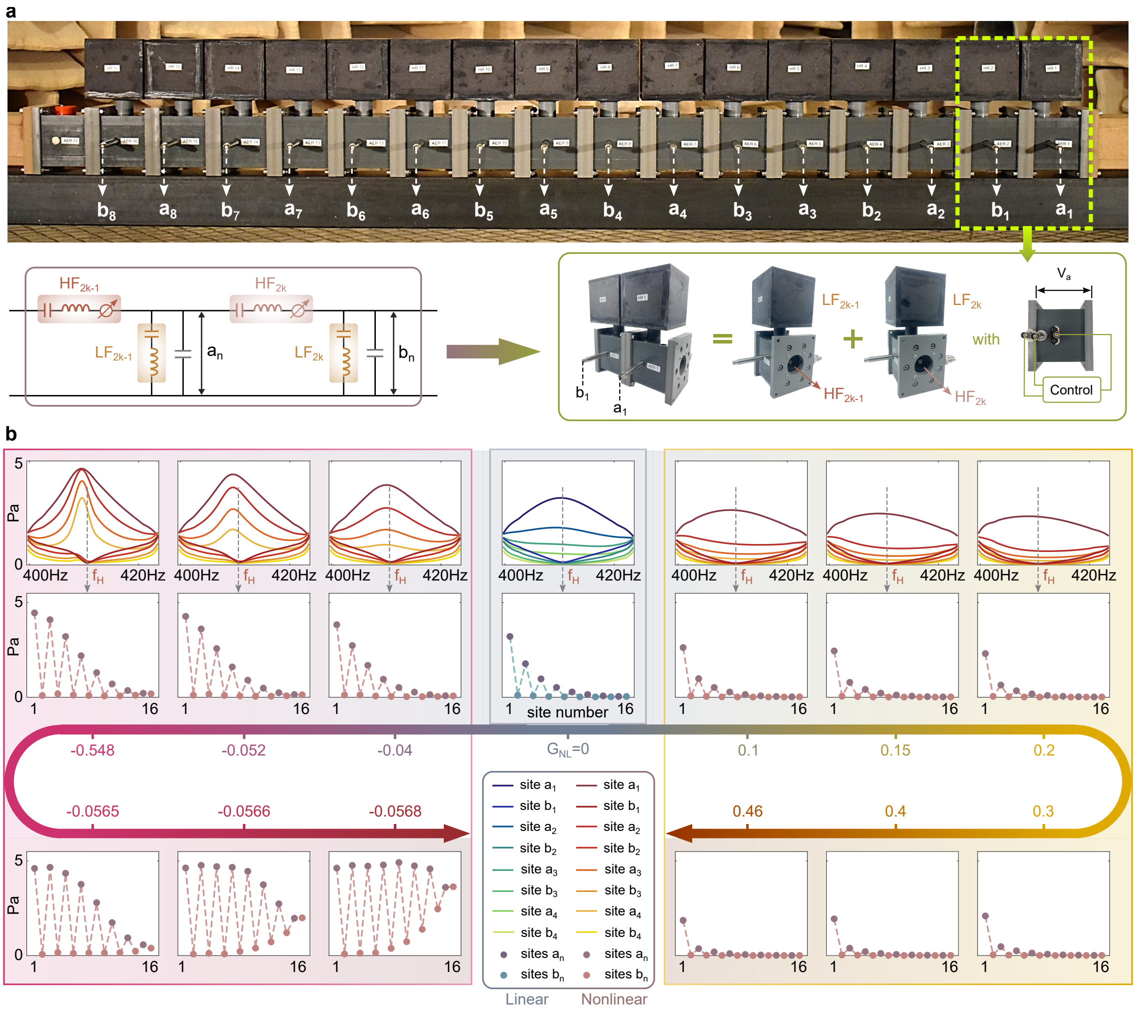

Figure 3: **Evolution of the chiral symmetry protected nonlinear topological edge state: experimental validation in an active nonlinear acoustic system.** (**a**) The actual system that realizes the theoretical lattice in Fig. 2a. The unit cell consists of two passive linear Helmholtz resonators (acting as LF_n) and two active nonlinear loudspeakers (acting as HF_n). The whole system starts and ends both with the controlled loudspeakers. The a_n and b_n correspond to the acoustic pressures applied to the Helmholtz resonators LF_{2k-1} and LF_{2k}, respectively. (**b**) Nonlinear topological edge states, measured as nonlinearity is progressively altered using the constant control parameter G_{NL}. The hopping ratios on sublattice A are increased (decreased) along $G_{NL} < 0$ ($G_{NL} > 0$). The edge state frequency f_H is identified from the spectra of a_i and b_i ($i = 1, 2, 3, 4$). Experimental results of more nonlinear cases are given in Fig. 13 in Appendix B.3.

The same investigations as in the theoretical studies are performed experimentally. First, the topological edge state is successfully implemented in the linear case, as illustrated in Fig. 3b (detailed linear results in Fig. 12 in Appendix B.3). A hopping ratio of around 0.54 is obtained, not very far from the theoretical one of 0.41 (Fig. 2b). The discrepancy stems from the approximation of each space V_a as a lumped element (Appendix A.6). Based on the linear results, nonlinearity is added to the system and tailored by the constant parameter G_{NL}, as theoretically set in Fig. 2b. When nonlinear magnitude is reinforced along $G_{NL} < 0$, the hopping ratios on A increase. The sites a_n sequentially attain the same level, enabling the theoretical plateau limit at the greatest extent of nonlinearity. In the meantime of the ascent on sublattice A, the sites in B first remain at rest and then rise in amplitude from the last one b_8, which comply also with the theoretical projections.

For nonlinearity decreasing the hopping ratios with $G_{NL} > 0$, the shape of the edge state is centralized more and more on the structure (left) end, with all sites in B staying stationary. The nonlinear variation along this direction proceeds until the first hopping ratio (the smallest one) on A falls to about 0.2, with respect to the linear one of 0.54. The limit of only a_1 being dynamic cannot be observed, as instability arises first, which is in accordance with time-domain analysis (Appendix B.2, Fig. 9). Nevertheless, all expected laws of variations are exhaustively justified by experiments. The realized nonlinear topological edge states are negligibly affected by losses in the system. They preserve topologically nontrivial phases and with unchanged frequency at f_H, since chiral symmetry is here rigorously obeyed by nonlinearity.

6 Conclusion

In this study, we explored the nonlinear possibilities for the persistence of topological nontriviality. We targeted the symmetry-protected topological class and put the emphasis on chiral symmetry. The condition to secure symmetry was first formulated for general nonlinear periodic systems. It was then applied to one-dimensional lattices in which zero-energy topological edge states were modified by arbitrary nonlinearities with chiral symmetry. The trajectories of their nonlinear evolution were predicted based on a monotonic amplitude dependence of the nonlinearities. The results show that chiral nonlinearities can consistently maintain the edge states in a topologically nontrivial phase, regardless of the explicit nonlinear form and magnitude. The derived nonlinear topological edge states were put into practice through the consideration of a concrete finite system, with theoretical representation in a lumped element circuit, and with numerical (Supplementary Materials, Section S2) and experimental implementations in an equivalent active nonlinear acoustic system. By virtue of chiral symmetry, our investigations reveal a broad class of nonlinearities that keep the topological attributes intact and the edge state frequency unshifted across all nonlinear magnitudes, opening up new avenues of thought for the continued study of nonlinear topology.

Acknowledgements

Author contributions R.F. and P.D. initiated and supervised the project. H.L. supervised the experimental work. X.G. established the theoretical modeling, performed the numerical simulations, designed the prototype, and carried out the measurements and data analysis. X.G. and M.P. set up the experiment. L.J. and P.D. developed the theory. X.G. and H.L. raised part of the funding that supported the experiment. All authors contributed to the writing of the manuscript and thoroughly discussed the results.

Funding information X.G., M.P., R.F., and H.L. acknowledge the Swiss National Science Foundation (SNSF) under grant No. 200020_200498. L.J. is funded by a PhD grant allocation Contrat doctoral Normalien.

A Methods

A.1 Achievement of a topological system with chiral symmetry

The dynamics of the lumped-element circuit in Fig. 2a is described by

$$\begin{cases} \Delta_t^{(HF)} q_{2k-1} = C_{2k-1}^{(HF)}(b_{n-1} - a_n) + G_{NL}C^{(HF)}(b_{n-1} + a_n)^2 (b_{n-1} - a_n), \\ \Delta_t^{(HF)} q_{2k} = C_{2k}^{(HF)}(a_n - b_n) - G_{NL}C^{(HF)}(a_n + b_n)^2 (a_n - b_n), \\ \Delta_t^{(LF)}\left(q_{2k-1} - q_{2k} - q_{2k-1}^{(a)}\right) = C_{2k-1}^{(LF)} a_n, \\ \Delta_t^{(LF)}\left(q_{2k} - q_{2k+1} - q_{2k}^{(a)}\right) = C_{2k}^{(LF)} b_n, \end{cases} \tag{A.1}$$

where $C^{(HF)}$ is the average of the capacitors $C_{2k-1}^{(HF)}$ and $C_{2k}^{(HF)}$.
The time-domain variables in Eq. A.1 are:
(I) The q_{2k-1}, q_{2k} and $q_n^{(a)}$ ($n = 2k-1$ and $n = 2k$), which denote the charges of the resonators HF_{2k-1}, HF_{2k} and the capacitor C_a in parallel with LF_n, respectively.
(II) The voltages applied to LF_{2k-1} and LF_{2k}, which correspond to the time responses of a_n and b_n in the topological dimerized lattice. The site amplitudes of the edge states in Fig. 2b are extracted at the frequency of the fundamental component, while higher harmonic generations are negligible in our system (less than 1% in all cases).
(III) The generators $V_{2k-1}^{(NL)}$ and $V_{2k}^{(NL)}$, which deliver voltages that comply with the desired nonlinearity given in Fig. 2a.
(IV), The time-domain differential operators $\Delta_t^{(HF)}$ and $\Delta_t^{(LF)}$, which read

$$\begin{cases} \Delta_t^{(HF)} = \left[M_{2k-1}^{(HF)} C_{2k-1}^{(HF)} \dfrac{d^2}{dt^2} + 1\right] = \left[M_{2k}^{(HF)} C_{2k}^{(HF)} \dfrac{d^2}{dt^2} + 1\right], \\ \Delta_t^{(LF)} = \left[M^{(LF)} C^{(LF)} \dfrac{d^2}{dt^2} + 1\right]. \end{cases} \tag{A.2}$$

Substituting Eq. (A.2) into Eq. (A.1) and eliminating all terms containing charges, the equations on voltages can be obtained as follows:

$$\begin{cases} \Delta_t a_n = \Delta_t^{(LF)}\left[C_1^{(HF)} b_{n-1} + C_2^{(HF)} b_n - C_1^{(HF)} V_{2k-1}^{(NL)} + C_2^{(HF)} V_{2k}^{(NL)}\right], \\ \Delta_t b_n = \Delta_t^{(LF)}\left[C_1^{(HF)} a_{n+1} + C_2^{(HF)} a_n + C_1^{(HF)} V_{2k+1}^{(NL)} - C_2^{(HF)} V_{2k}^{(NL)}\right], \end{cases} \tag{A.3}$$

with $\Delta_t = \Delta_t^{(HF)}\Delta_t^{(LF)} C_a + \Delta_t^{(HF)} C^{(LF)} + 2C^{(HF)}\Delta_t^{(LF)}$, and with $C_1^{(HF)} = C_{2k-1}^{(HF)}$, $C_2^{(HF)} = C_{2k}^{(HF)}$, $C^{(HF)} = (C_1^{(HF)} + C_2^{(HF)})/2$.

If $\Delta_t = 0$ is possible, then Eq. (A.3) leads to

$$\begin{cases} 0 = t_{1b}(b_{n-1}, a_n)\, b_{n-1} + t_{0b}(b_n, a_n)\, b_n, \\ 0 = t_{1a}(a_{n+1}, b_n)\, a_{n+1} + t_{0a}(a_n, b_n)\, a_n, \end{cases} \tag{A.4}$$

The Eq. A.4 satisfies the general description of 1D chiral topological systems in Eq. 2, where the hopping terms t_{1b}, t_{1b}, t_{1b} and t_{1b} are expressed explicitly as follows,

$$\begin{cases} t_{1a}(a_{n+1}, b_n) = C_1{}^{(HF)} + G_{NL}C^{(HF)}\left(a_{n+1}^2 + b_n a_{n+1} - b_n^2\right), \\ t_{0a}(a_n, b_n) = C_2{}^{(HF)} - G_{NL}C^{(HF)}\left(a_n^2 + b_n a_n - b_n^2\right), \\ t_{1b}(b_{n-1}, a_n) = C_1{}^{(HF)} + G_{NL}C^{(HF)}\left(b_{n-1}^2 + a_n b_{n-1} - a_n^2\right), \\ t_{0b}(b_n, a_n) = C_2{}^{(HF)} - G_{NL}C^{(HF)}\left(b_n^2 + a_n b_n - a_n^2\right), \end{cases} \tag{A.5}$$

with $C_1{}^{(HF)} = C_{2k-1}^{(HF)}$ and $C_2{}^{(HF)} = C_{2k}^{(HF)}$. Accordingly, the hopping ratios $\eta_L + \eta_{NLa}$ and $\eta_L + \eta_{NLb}$ can be obtained from

$$\eta_L + \eta_{NLa} = \frac{t_{0a}(a_n, b_n)}{t_{1a}(a_{n+1}, b_n)}, \quad \eta_L + \eta_{NLb} = \frac{t_{0b}(b_n, a_n)}{t_{1b}(b_{n-1}, a_n)}. \tag{A.6}$$

The derivation from Eq. (A.3) to (A.4) implies that, if the higher harmonic generations are negligible in the system, topological edge states can be achieved at the fundamental frequencies in the presence of a solution for $\Delta_t = 0$. This is exactly the case in our system, where the higher harmonic generations are consistently lower than 1%. All the edge state profiles shown in this study refer to the absolute amplitudes of the fundamental components of a_n and b_n. Interestingly, two frequencies allow $\Delta_t = 0$, i.e., the topological edge states are attained at two different frequencies in our system, see Fig. 4 in Appendix B.1 for physical explanations.

A.2 Boundary conditions

Theoretically, for the edge state generations, we require that the boundaries b_0 and a_e of the lumped element circuit in Fig. 2a satisfy $b_0 = a_e = 0$. However, this is not directly achievable in practice, especially for the acoustic system we chose for the experiments. In our search for applicable boundary conditions, we eventually found that the typical Non-Reflecting Boundary Conditions (NRBCs) in planar acoustic wave propagation can replace the ideal ones, as proved in Fig. 5 in Appendix B.1. They are thus undertaken for all the studies of the concrete theoretical model and the equivalent experimental system.

A.3 Methods for theoretical solvings

To solve the problem associated with the circuit in Fig. 2a, we consider the original dynamic equations in Eq. A.1 where all the variables are time-dependent. Two standard methods are exploited for solving these nonlinear differential equations, namely the harmonic balance method [56–58] and the time-integration method [59]. They are capable of handling strong levels of nonlinearities, in contrast to the perturbation method and the method of multiple scales that are valid only at weak nonlinearities.

The Harmonic Balance Method (HBM) refers to a semi-analytical method [56–58] which determines the steady-state solutions of the nonlinear problem. The first 27 harmonics of each variable are taken into account when solving Eq. A.1. The outcomes show that the higher harmonic generations are lower than 1% in our system. The a_n and b_n in Fig. 2b correspond to the absolute amplitudes of their fundamental harmonic components (at the edge state frequency f_H). The detailed results (more nonlinear cases than in Fig. 2b) are summarised in Fig. 6 in Appendix B.1.

The time integration method, with the fourth-order Runge-Kutta (RK4), is utilized to solve the problem directly in the time domain, which accounts for the transient responses. The relevant results are given in Fig. 7 in Appendix B.1.

A.4 Time-domain simulation of the experiments.

To better guide and analyze the experiments, we performed time-domain simulations for the active nonlinear acoustic system built in practice (Fig. 3a). The approach involves a Finite Difference Time Domain (FDTD) method by discretization of the 1D wave equations. Practical details are accounted for in the simulations, that is (i) we consider the wave propagation inside each space between two nearby loudspeakers (with FDTD), (ii) we add the losses in all resonant elements and transmission lines according to the experimentally estimated values, (iii) the actual active control on each loudspeaker, with the control principle and laws explained in the following section for experiments (Eqs. (A.7) and (A.8) with $\mathrm{i(t)}$ changing to $\mathrm{i}(\mathrm{t}-\tau)$, and with $\tau = 100\,\mu\mathrm{s}$). Regarding the numerical settings, we randomly take the experimental values of one loudspeaker to define all the others. The simulation outcomes are summed up in Fig. 9 in Appendix B.2. They are essentially identical to the experimental ones.

A.5 Characterisations of the experimental setup

In the experimental setup (Fig. 3a), the non-reflecting boundary conditions are achieved with anechoic terminations at both ends of the system, which are qualified by absorption coefficients higher than 0.998 from 140 Hz (less than 5% of reflection). The waveguide refers to a PVC duct with a cross-sectional area of 6 cm × 6 cm, which ensures planar wave propagation until 2.86 kHz. The manufactured Helmholtz resonators (labeled with HR_n in Fig. 3a) reach a transmission coefficient of around 0.008 at their resonance frequencies in the range of [110.5 Hz, 111.5 Hz], corresponding to an acoustic resistance of $0.005\mathrm{Z_c}$ with $\mathrm{Z_c}$ the specific acoustic impedance of the air. The electrodynamic loudspeakers are all the same commercially available Visaton FRWS 5 SC model, while they possess different resonance frequencies (within [345 Hz, 375 Hz]) and bandwidths, which we calibrated beforehand.

A.6 Active control on the electrodynamic loudspeakers.

The loudspeaker membrane behaves as a mass-spring-damper system in the linear regime (weak input levels). The motion equation for its displacement ξ read

$$\mathrm{M_{ms}}\frac{\partial^2}{\partial \mathrm{t}^2}\xi(\mathrm{t}) + \mathrm{R_{ms}}\frac{\partial}{\partial \mathrm{t}}\xi(\mathrm{t}) + \frac{1}{\mathrm{C_{ms}}}\xi(\mathrm{t}) = \mathrm{p_{tot}(t)S_d} - \mathrm{Bli(t)}, \tag{A.7}$$

In the passive open-circuit case, the membrane is subject to the total acoustic pressure $\mathrm{p_{tot}}$ over its effective surface area $\mathrm{S_d}$, and the mechanical forces which rely on the mechanical mass $\mathrm{M_{ms}}$, resistance $\mathrm{R_{ms}}$, and compliance $\mathrm{C_{ms}}$. Its dynamics are characterized by a specific acoustic impedance $\mathrm{Z_s}$ (ratio between acoustic pressure and velocity) in the frequency domain, $\mathrm{Z_s}(\mathrm{j}\omega) = \frac{1}{\mathrm{S_d}}\left(\mathrm{j}\omega\mathrm{M_{ms}} + \mathrm{R_{ms}} + \frac{1}{\mathrm{j}\omega\mathrm{C_{ms}}}\right)$.

The active control on each loudspeaker is implemented by specifying the current $\mathrm{i(t)}$, which creates an electromagnetic force through the moving coil with a force factor of Bl. The control approach is depicted in detail in Fig. 11, where the control law is digitally defined with a Speedgoat real-time target machine manipulated in the Simulink environment of MATLAB. It produces the current $\mathrm{i(t)}$ in the form of,

$$\mathrm{i(t)} = \mathcal{F}^{-1}\left(\Phi(\mathrm{j}\omega)\cdot \mathrm{P_{tot}}(\mathrm{j}\omega)\right) + \mathcal{F}^{-1}\left(\frac{\mathrm{S_d}}{\mathrm{Bl}} - \Phi(\mathrm{j}\omega)\right) * \left((-1)^n \frac{\mathrm{C}^{(\mathrm{exp})}}{\mathrm{C}_n^{(\mathrm{exp})}}\mathrm{G_{NL}p_{tot}(t)}\left(\mathrm{p_f(t)} + \mathrm{p_b(t)}\right)^2\right), \tag{A.8}$$

where $\mathrm{p_f}$ and $\mathrm{p_b}$ are the acoustic pressures measured at the front and rear faces of the loudspeaker membrane, which are the two inputs for the control. $\mathcal{F}^{-1}$ and the symbol $*$ designate the inverse of the Fourier Transform and the time convolution, respectively. The total acoustic pressure p_{tot} reads $p_{tot} = p_f(t) - p_b(t)$, with $P_{tot} = \mathcal{F}(p_{tot})$ its Fourier transform. $C_n^{(exp)}$ refers to the acoustic compliance achieved for the n-th loudspeaker which differs between $n = 2k-1$ and $n = 2k$, and $C^{(exp)}$ is the average of two successive ones, they are equivalent to the electrical capacitors $C_1^{(HF)}$ for $n = 2k-1$, $C_2^{(HF)}$ $n = 2k$, and $C^{(HF)}$ in Eq. (A.1).

In Eq. (A.8), the linear part of control is represented by a linear transfer function $\Phi(j\omega)$, whereas the nonlinear part is determined by the parameter G_{NL}. For the linear part, $\Phi(j\omega)$ is used to tailor the impedance properties of the loudspeaker,

$$\Phi = \frac{S_d}{Bl} \cdot \beta \, \frac{Z_{st}(j\omega) - Z_s(j\omega)}{Z_{st}(j\omega)}. \tag{A.9}$$

It targets a specific acoustic impedance $Z_{st}^{(F)}$ with two degrees of freedom,

$$Z_{st}^{(F)} = \frac{Z_{st}\, Z_s}{(1-\beta)\, Z_{st} + \beta\, Z_s} = \left[\frac{1-\beta}{Z_{st}} + \frac{\beta}{Z_s} \right]^{-1}, \tag{A.10}$$

in which the control-designed impedance Z_{st} corresponds to a one-degree-of-freedom resonator. It is made in parallel with the passive one Z_s, while their weights are adjusted by the constant parameter β.

For the control execution, there exists a time delay τ from control inputs to outputs, which is unavoidable in reality. It is taken into account in simulating the practical case by transforming $i(t)$ into $i(t-\tau)$ for Eq. (A.7), and is experimentally determined at $100\,\mu s$. Since the loudspeakers are naturally different, the control time delay affects them differently, yielding discrepancies in control results. Nevertheless, the addition of the parameter β in the linear control law allows such an issue to be compensated for in experiments, by balancing between Z_{st} and Z_s. Fig. 12 in Appendix B.1 shows the results for linearly generated topological edge state.

As for the nonlinear part of the control law in Eq. (A.8), when the sub-wavelength cavity V_a between adjacent loudspeakers exhibits predominantly capacitor characteristics (the assumption under consideration, see Fig. 3a), we have $p_f = b_{n-1}$ and $p_b = a_n$ for loudspeakers with even indexes, and $p_f = a_n$ and $p_b = b_n$ for those with odd indexes. In this case, the nonlinear laws perfectly achieve the generators V_{2k-1}^{NL} and V_{2k}^{NL} required in the theoretical lattice in Fig. 2a.
Performing the above hybrid (linear and nonlinear) control on each loudspeaker, they all become Active Electroacoustic Resonators [60–63] (labeled with AER_n in Fig. 3a), presenting the desired properties for realizing HF_n. A low level of less than 1 Pa is maintained for system excitation. It ensures the linear behaviors of the loudspeakers in the passive (control off) regime. Thus, nonlinearity is generated and tuned in an exact way, i.e., through the active control only (using the constant parameter G_{NL} in the control law). The time responses of a_n and b_n are measured by the microphones below Helmholtz resonators, as indicated in Fig. 3a. The edge states shown in Fig. 3b refer to their components at the fundamental frequency (edge state frequency f_H). We confirm with measurements that the higher harmonic generations are consistently less than 1% in our acoustic system, which is in line with the theoretical model. The detailed experimental results of nonlinear topological edge states are provided in Fig. 13 in Appendix B.3. The cases where nonlinearities break chiral symmetry are investigated in Appendix B. Figs. 8, 10 and 14 show the corresponding theoretical, numerical, and experimental results, respectively.

B Supplementary results

Here in the Appendix B.1, B.2 and B.3, we show supplementary results for the theoretical study of the lumped-element model in section 4, the time-domain simulation of the actual acoustic system, and the experimental realization in section 5, respectively.

B.1 Theoretical results

This section includes:
Fig. 4: Principle and physical explanations for the generation of dual-band topological edge states in our lumped-element system.
Fig. 5: Proof of the equivalence between the theoretically ideal boundary conditions (Fig. 5b) and the non-reflecting ones (Fig. 5c) that are more realizable for our acoustic experiments.
Fig. 6: Detailed theoretical results obtained by solving Eq. (A.1) with the Harmonic Balance Method (HBM). More cases are shown compared to Fig. 2 in the main text.
Fig. 7: Theoretical results obtained by solving solving Eq. (A.1) with the time integration method (fourth-order Runge-Kutta).
Figs. 8: Theoretical results for two cases where nonlinearities break chiral symmetry. They are in comparison with the simulation outcomes in Fig. 10 and the experimental ones in Fig. 14, where the same forms of nonlinearities are considered.

B.2 Simulation results

This section includes
Fig. 9: Detailed time-domain simulation results of the realized nonlinear topological edge states. Notably, practical situations are accounted for in the simulation (Appendix A.4), where the pressure is not precisely homogeneous in the cavity, and the control uses the pressures close to each loudspeaker as inputs (Appendix A.6). By contrast, the theoretical study assumes that the cavity between successive HF_n behaves as a capacitor, thus presenting the same pressure over it. This eventually causes a difference in hopping ratios in the two studies. In theoretical results, the hopping ratio of the linear edge state is around 0.41, corresponding to the compliance ratio between $\mathrm{C}_2^{(\mathrm{HF})}$ and $\mathrm{C}_1^{(\mathrm{HF})}$. Whereas the linear hopping ratio obtained in simulations is equal to 0.52 (0.54 in experiments), larger than the theoretical value.
Fig. 10: Simulation results for two cases where nonlinearities break chiral symmetry. They are in comparison with the theoretical ones in Fig. 8 and the experimental ones in Fig. 14, where the same forms of nonlinearities are considered.

B.3 Experimental results

This section includes
Fig. 11: Principle of the real-time feedback control applied to electrodynamic loudspeakers.
Fig. 12: Experimental results of the topological edge state at $\mathrm{f_H}$ in the linear regime.
Fig. 13: Detailed experimental results of the realized nonlinear topological edge states. More nonlinear cases are shown compared to Fig. 3.
Fig. 14: Experimental results for cases where nonlinearities break chiral symmetry. They are in comparison with the theoretical ones in Fig. 8 and the simulation ones in Fig. 10, where the same forms of nonlinearities are considered.

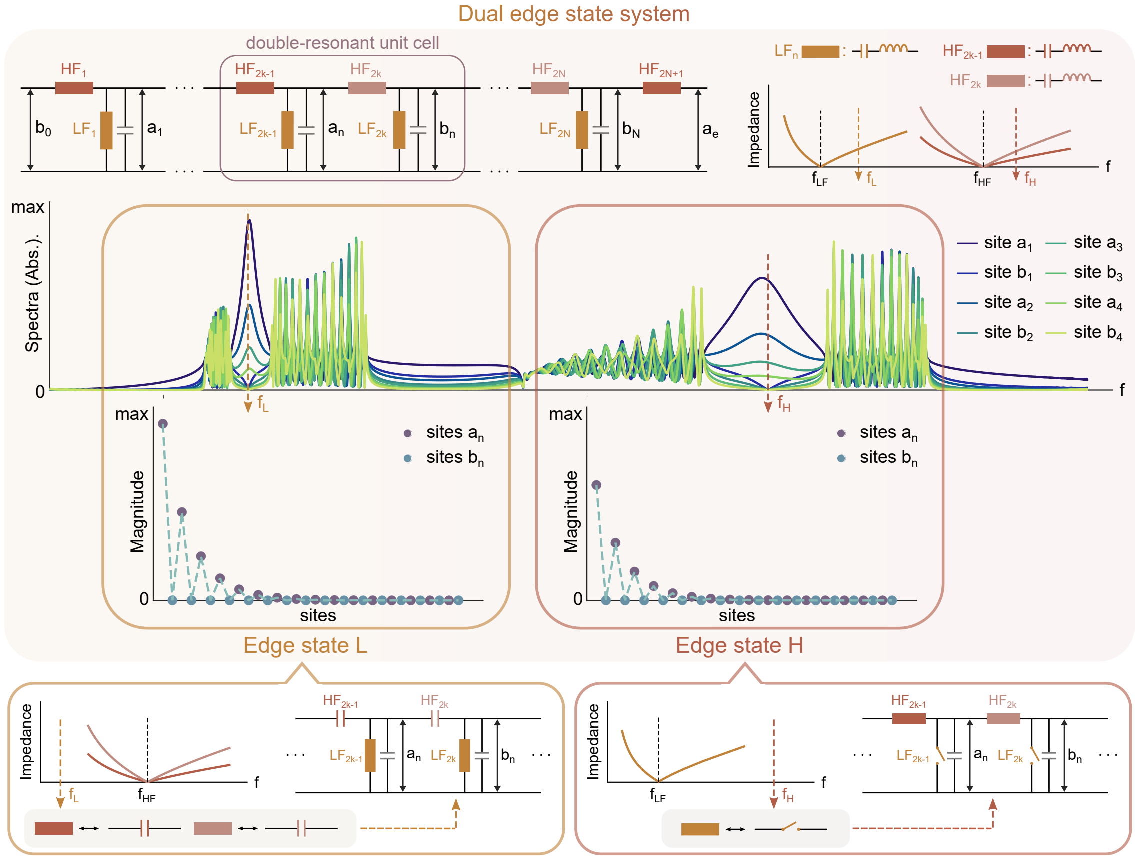

Figure 4: **Dual-band topological edge states in a single finite system.** Each unit cell (with index n) of the system includes 2 types of resonators, (i) identical resonators LF_n ($n = 2k-1$ and $2k$) resonating at a frequency $\mathrm{f_{LF}}$, and (ii) resonators HF_n resonating at $\mathrm{f_{HF}}$ higher than $\mathrm{f_{LF}}$, but with different resonance bandwidths between odd (HF_{2k-1}) and even (HF_{2k}) ones. In the linear regime where all HF_n possess no nonlinearities, with $\mathrm{f_{LF}} < \mathrm{f_{HF}}$, the resonators HF_n exhibit mainly capacitance characteristics in the vicinity of $\mathrm{f_{LF}}$, leading to the manifestation of only the resonance of LF_n in the unit cell. Similarly, when close to the frequency $\mathrm{f_{HF}}$ which is far from $\mathrm{f_{LF}}$, the resonators LF_n have barely any impact, only the resonance of HF_n can act. Therefore, our system is equivalent to a classic topological lattice made of single-resonant unit cells at two different frequencies, denoted as $\mathrm{f_L}$ and $\mathrm{f_H}$, respectively, as delineated in this figure. Their mathematical derivations are provided in Appendix A.1. After introducing arbitrary nonlinearities, the linearly achieved topological edge states can persist and remain intact at these two frequencies, provided that the chiral symmetry is consistently satisfied, as we proved in the main text.

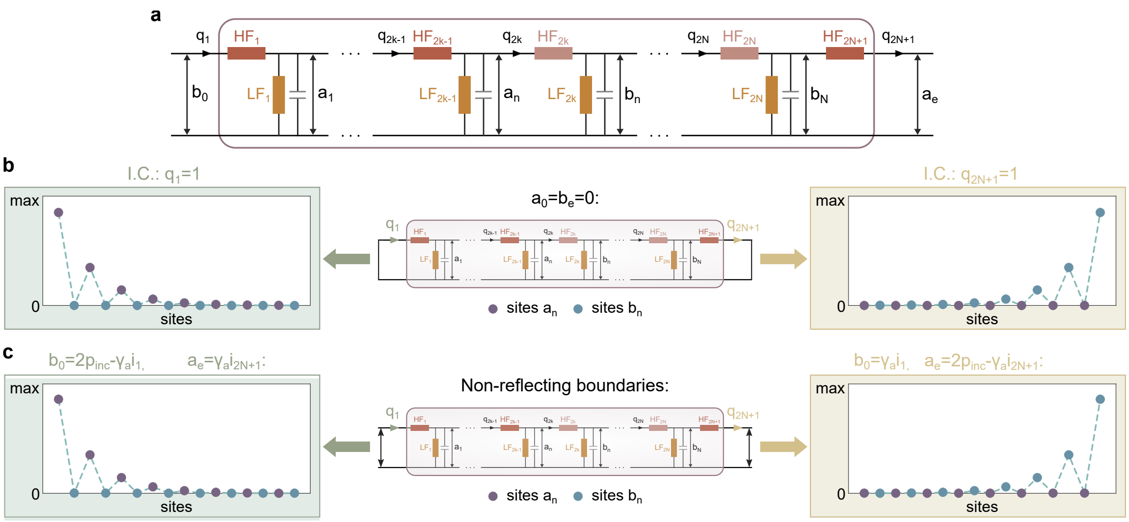

Figure 5: **Identification of realizable boundary conditions.** (**a**) The lumped element circuit considered, with b_0 and a_e the input and output boundaries, respectively. q_n designates the charge of the resonator HF_n. (**b**) Zero-energy topological edge state at f_H derived with the ideal closed-closed boundary conditions ($b_0 = a_e = 0$), and with a nonzero initial conditions of $q_1 \neq 0$ (left inset) or $q_{2N+1} \neq 0$ (right inset), respectively. (**c**) Zero-energy topological edge state at f_H derived with the Non-Reflecting Boundary Conditions (NRBCs) for both ends of the system, where excitation is defined at each end, respectively. Based on an electro-acoustic analog where electrical (voltage, current) is equivalent to acoustic (pressure, flow), NRBCs are translated into $a_e = \gamma_a i_{2N+1}$ ($b_0 = \gamma_a i_1$) for the right (left) end of the system, in which i_{2N+1} (i_1) represents the current circulating in HF_1 (HF_{2N+1}), and $\gamma_a = Z_c/S$ with Z_c the specific acoustic impedance of the air and S the surface area of the propagation medium. The planar wave excitation at the left (right) end of the system can be expressed by the total pressure in the form of $b_0 = 2p_{inc} - \gamma_a i_1$ ($a_e = 2p_{inc} - \gamma_a i_{2N+1}$), with p_{inc} the incoming source that comes from infinity (there is no reflection in the direction of incidence). All results are obtained with the 4-th order Runge-Kutta. They evidence the equivalence between the two types of boundary conditions. In this study, we opt for the NRBCs in (**c**) which is more realizable in our acoustic experiments.

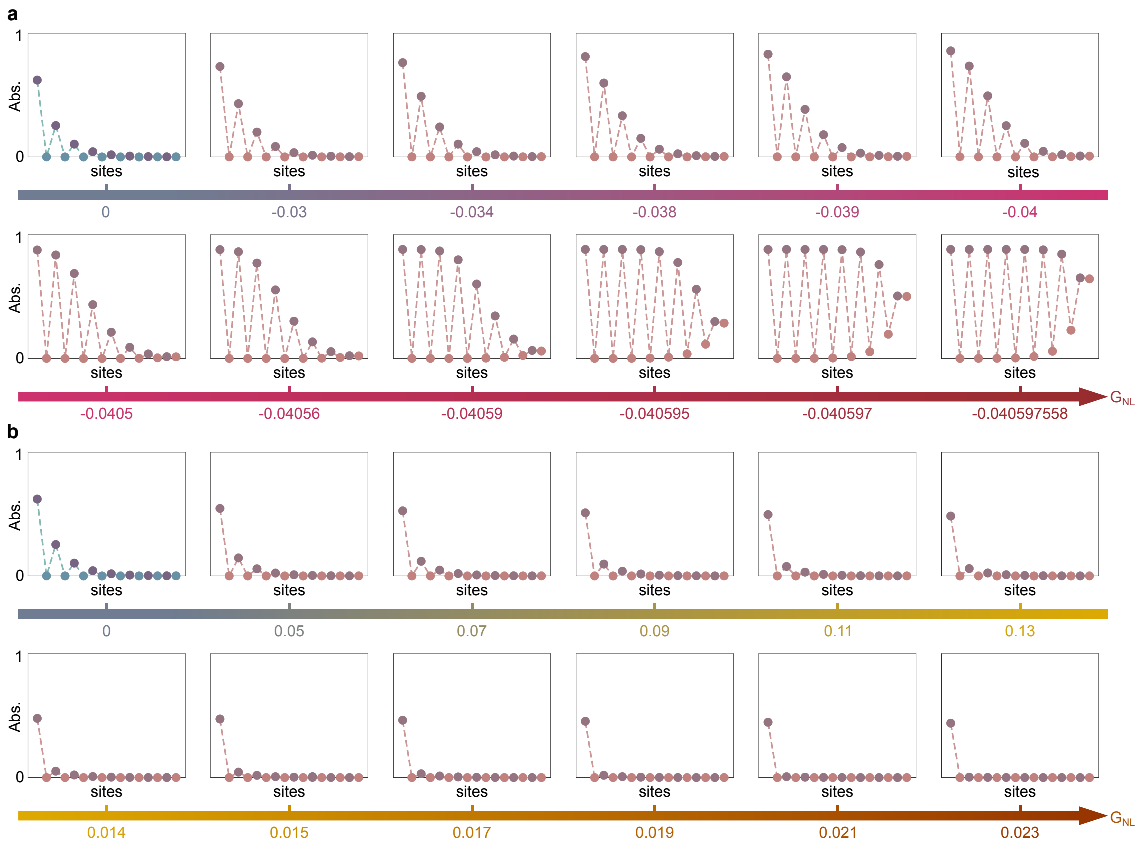

Figure 6: **Evolution of the chiral symmetry protected nonlinear topological edge states: detailed theoretical results.** The solutions are obtained with the Harmonic Balance Method (A.3). The level of nonlinearity is tuned using the constant parameter G_{NL}, the value of which varies in the negative (**a**) and positive (**b**) directions, respectively. All inset figures are displayed within the same amplitude range as in Fig.2 in the main text, while results of more nonlinear cases are showcased here.

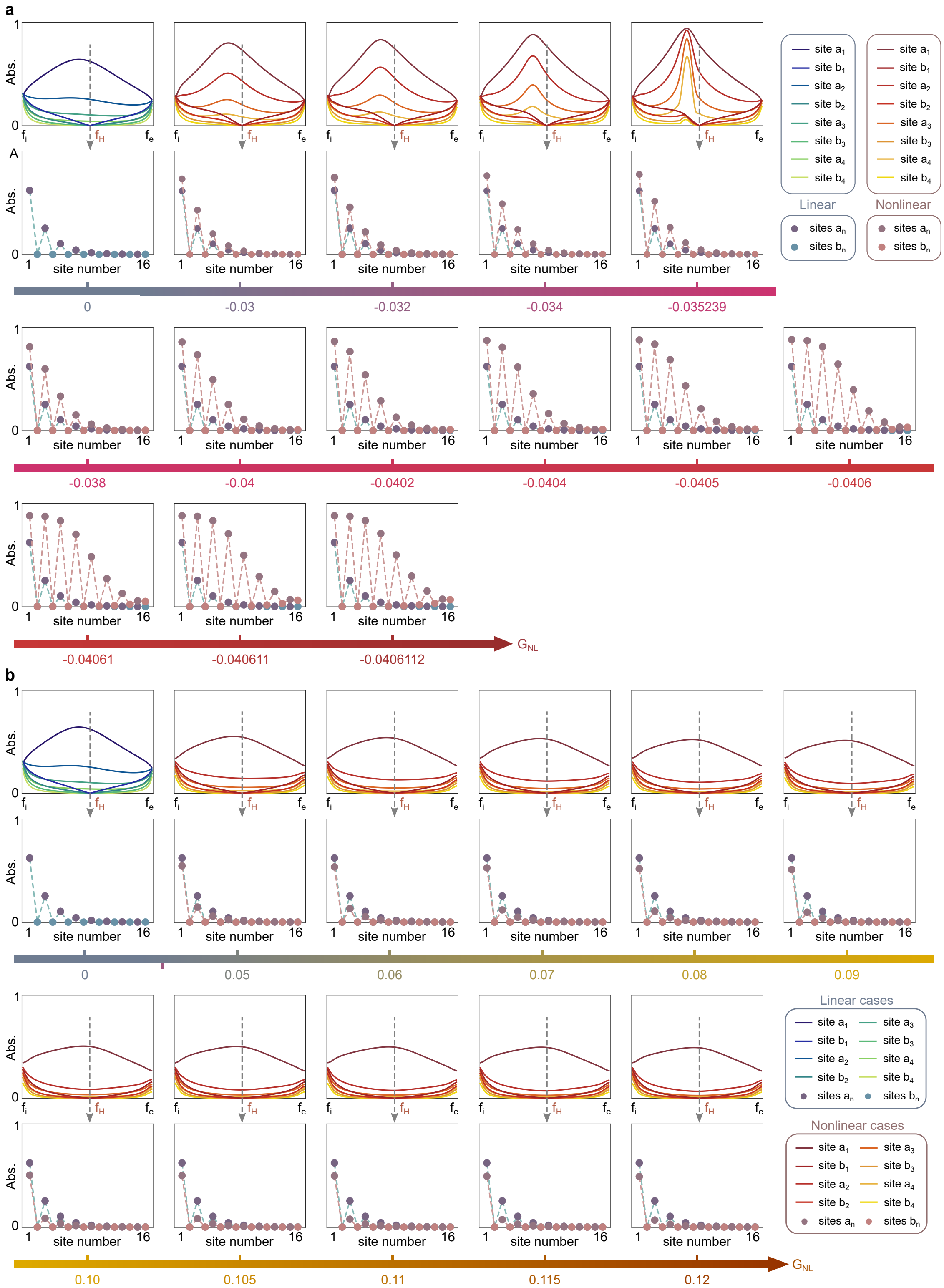

Figure 7: **Evolution of the chiral symmetry protected nonlinear topological edge states: results obtained with the time integration method (fourth-order Runge-Kutta).** Cases of $G_{NL} < 0$ and $G_{NL} > 0$ are summarized in (**a**) and (**b**), respectively. The evolutionary trends of the nonlinear edge state are consistent with those obtained with HBM (Fig. 6), except that the limit cases cannot be reached on account of the transition process. We demonstrate with simulations that reaching the plateau limit is actually possible (Appendix B.2, Fig. 9), as the hopping ratios are caused larger in the practical realizations.

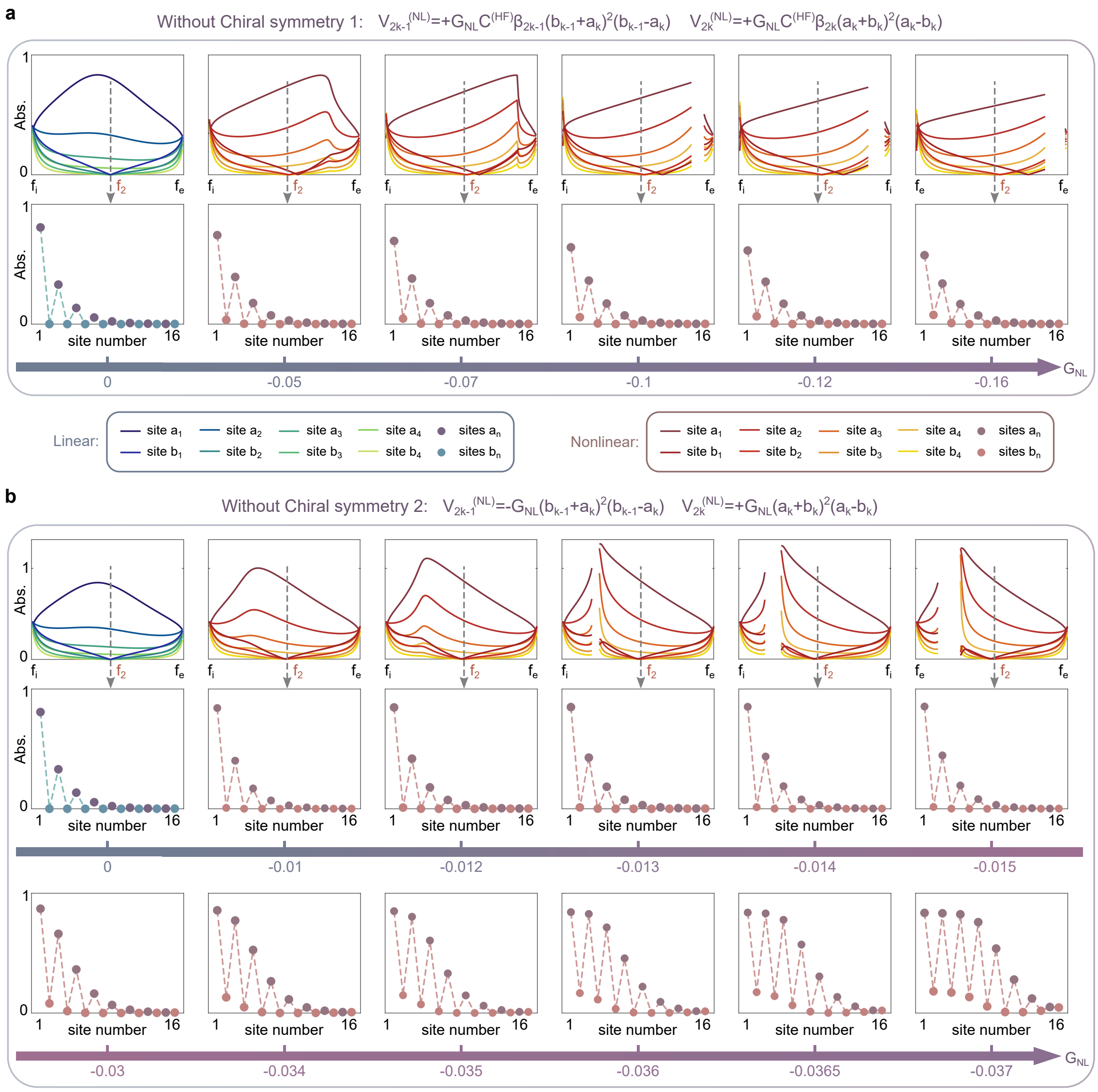

Figure 8: **Evolution of nonlinear topological edge state when nonlinearities break chiral symmetry: theoretical results.** Two forms of nonlinearities are investigated in (**a**) and (**b**), respectively. Results agree well with the numerical outcomes in Fig. 10 and the experimental ones in Fig. 14 where the same forms of nonlinearities are considered. They show that breaking chiral symmetry produces couplings between the two sublattices A and B, which causes the edge state to be shifted in frequency and distorted in shape.

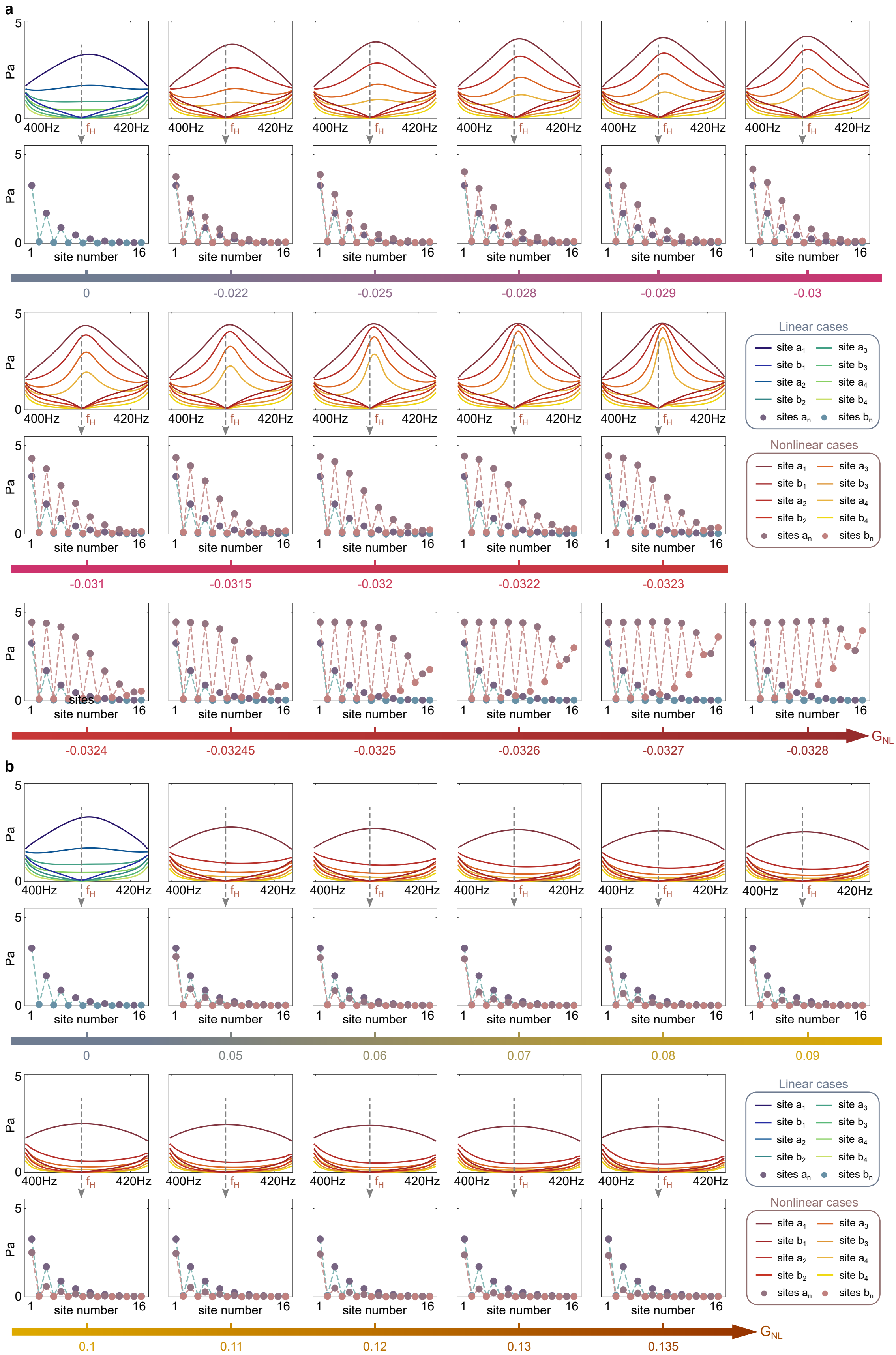

Figure 9: **Time-domain simulation results.** Results derived from time-domain simulation of the actual acoustic system. Nonlinearity adheres to chiral symmetry. The hopping ratios are (**a**) increased along $G_{NL} < 0$, and decreased along $G_{NL} > 0$, respectively.

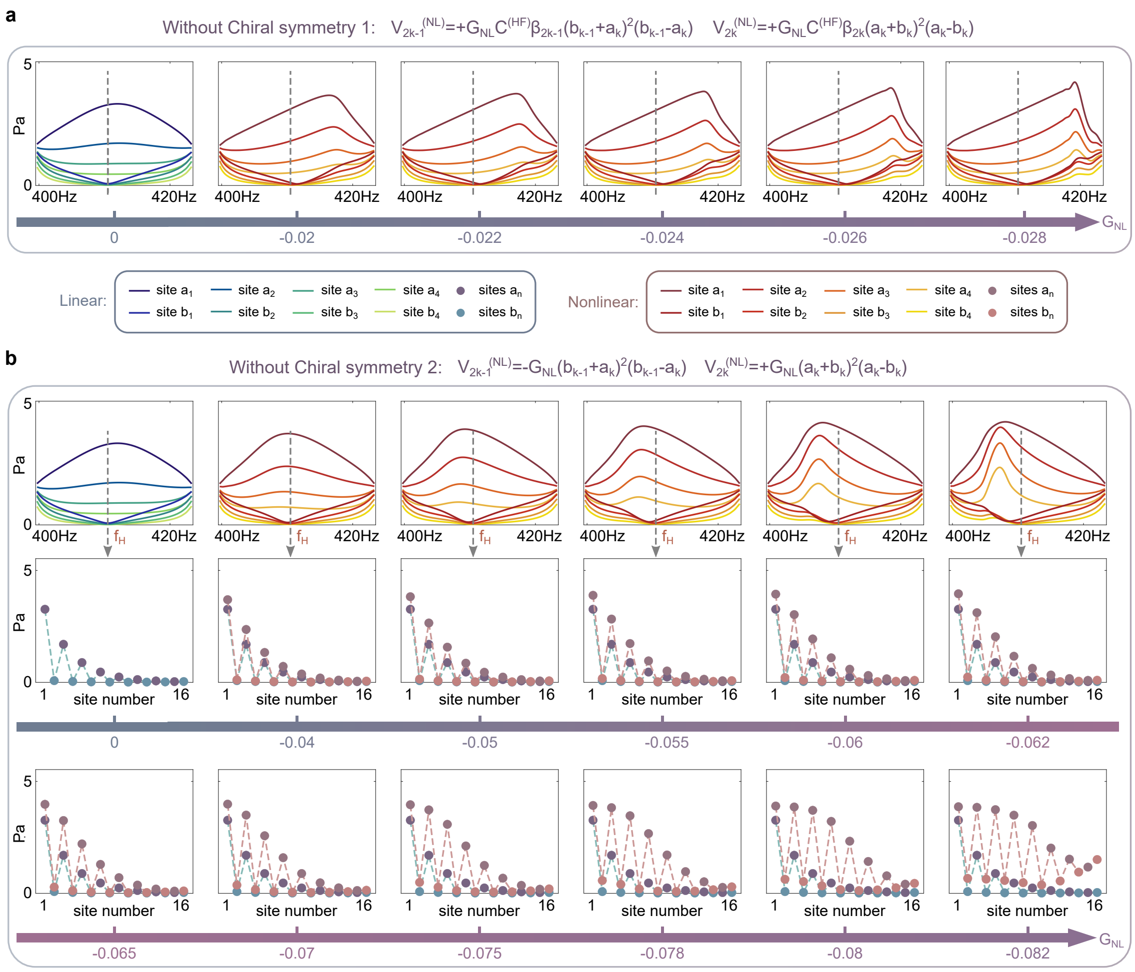

Figure 10: **Evolution of nonlinear topological edge state when nonlinearities break chiral symmetry: simulation results.** The actual acoustic system is simulated in the time domain. Two forms of nonlinearities are investigated in (**a**) and (**b**), respectively. Results agree well with the theoretical outcomes in Fig. 8 and the experimental ones in Fig. 14 where the same forms of nonlinearities are considered. They show that breaking chiral symmetry produces couplings between the two sublattices A and B, which causes the edge state to be shifted in frequency and distorted in shape.

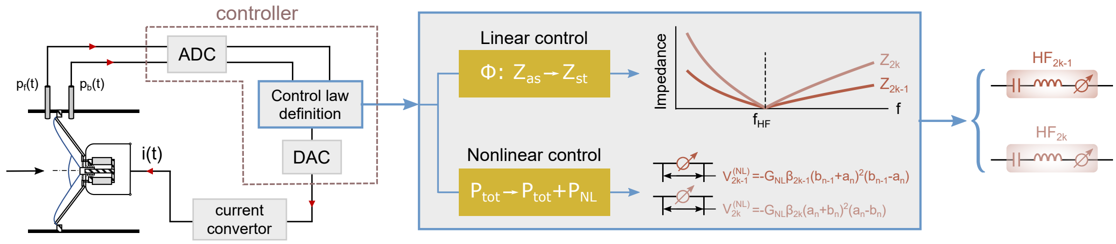

Figure 11: **Active control on the loudspeakers.** The linear part of the control is used for altering the impedance Z_n of each loudspeaker to make them resonate at the same frequency while achieving different resonance bandwidths between odd and even ones. The nonlinear part of the control is for producing the nonlinear generators $V_n^{(NL)}$ needed in the theoretical lattice in Fig. 2a. ADC (DAC) denotes the Analog-Digital (Digital-Analog) Converter. There exists a control time delay that is mainly due to the AD and DA conversions and thus unavoidable for the control law definition. We compensate for this delay effect by carefully defining the control laws, see implementation details in Appendix A.6.

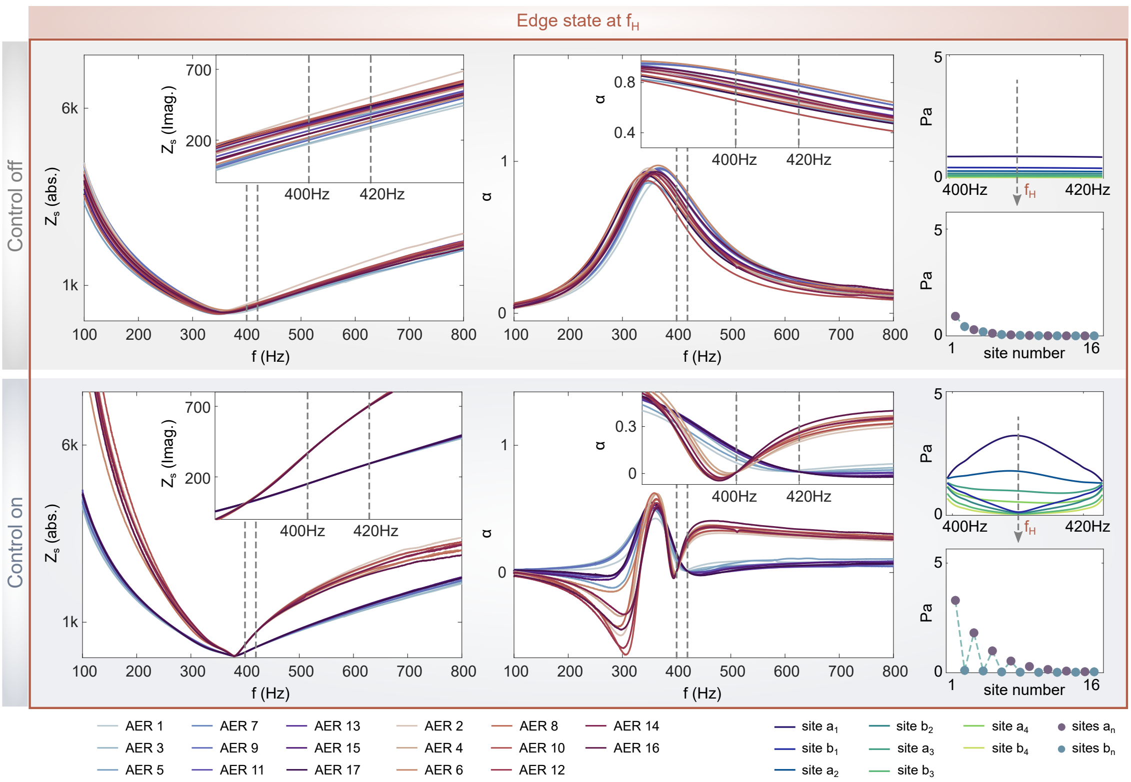

Figure 12: **Linear control results of topological edge state at f_H.** Comparison between the cases of control off and control on. The measured specific acoustic impedance Z_S and absorption coefficient α are also illustrated in both cases, for all the 17 loudspeakers in use. The edge state is linearly generated without distortions.

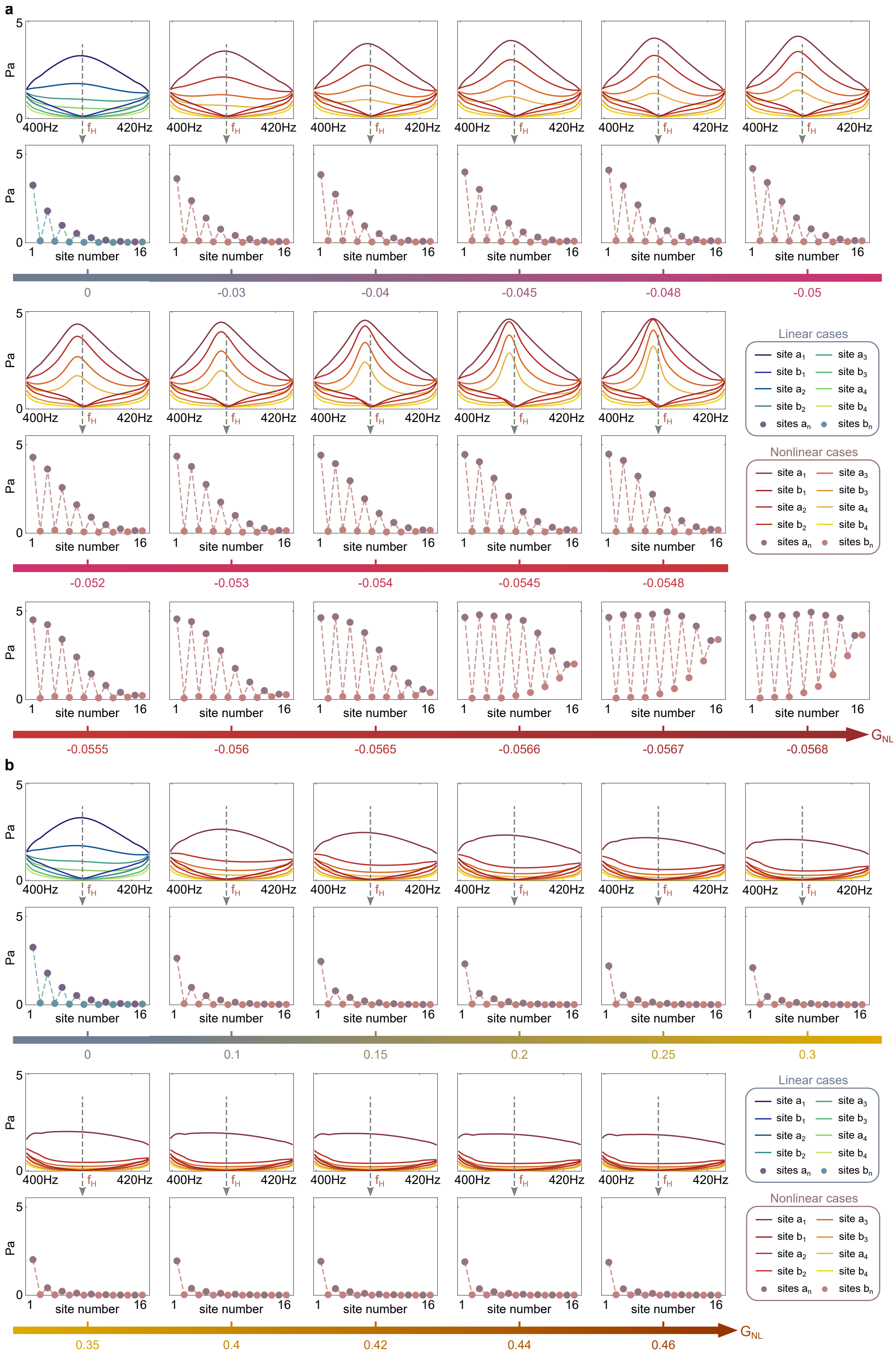

Figure 13: **Evolution of the chiral symmetry protected nonlinear topological edge states: detailed experimental results.** More results are given here compared to Fig. 3 in the main text, for (**a**) $G_{NL} < 0$ and (**b**) $G_{NL} > 0$, respectively.

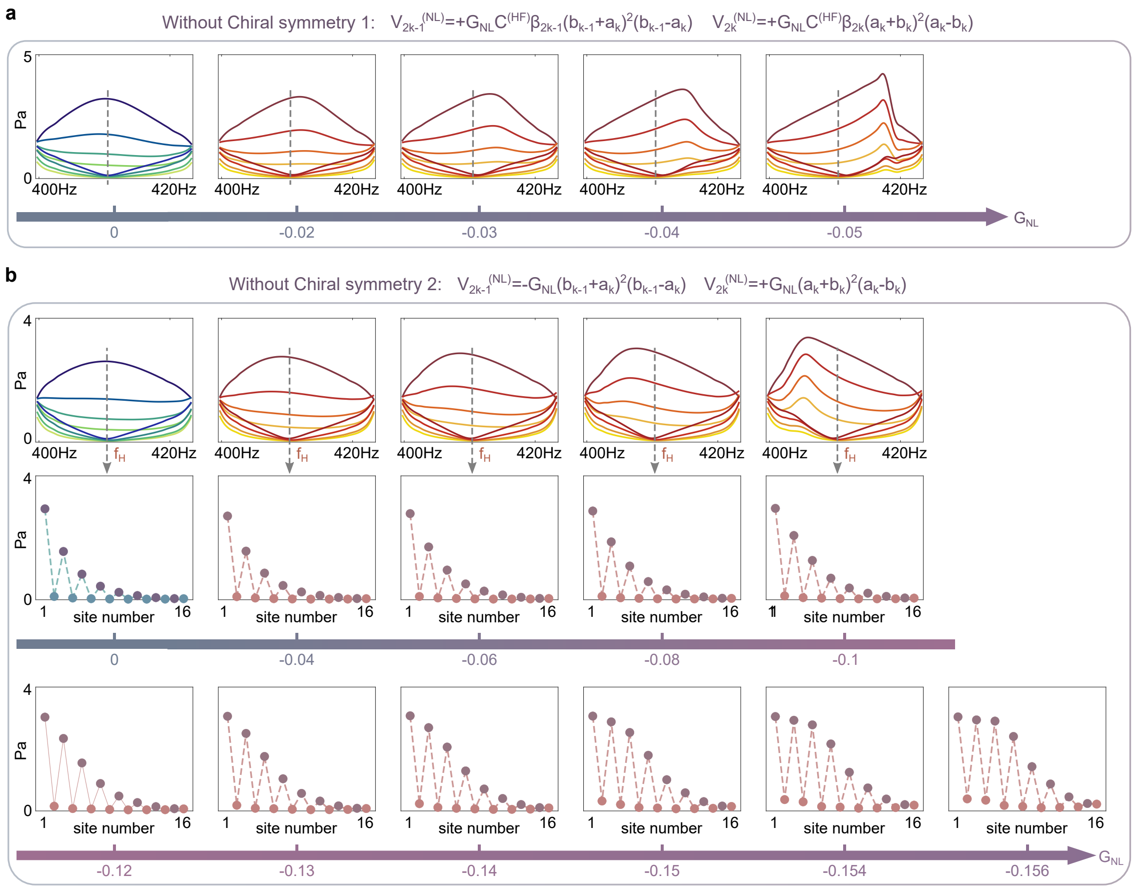

Figure 14: **Evolution of nonlinear topological edge state when nonlinearities break chiral symmetry: experimental results.** Two forms of nonlinearities are investigated in (**A**) and (**B**), respectively. Results agree well with the theoretical outcomes in Fig. 8 and the numerical ones in Fig. 10 where the same forms of nonlinearities are considered. They show that breaking chiral symmetry produces couplings between the two sublattices A and B, which causes the edge state to be shifted in frequency and distorted in shape.

References

[1] M. Z. Hasan and C. L. Kane, *Colloquium: Topological insulators*, Rev. Mod. Phys. **82**, 3045 (2010), doi:10.1103/RevModPhys.82.3045.

[2] S. N. Kempkes, M. R. Slot, J. J. van den Broeke, P. Capiod, W. A. Benalcazar, D. Vanmaekelbergh, D. Bercioux, I. Swart and C. M. Smith, *Robust zero-energy modes in an electronic higher-order topological insulator*, Nat. Mater. **18**, 1292–1297 (2019), doi:10.1038/s41563-019-0483-4.

[3] S. Imhof, C. Berger, F. Bayer, J. Brehm, L. W. Molenkamp, T. Kiessling, F. Schindler, C. H. Lee, M. Greiter, T. Neupert and R. Thomale, *Topolectrical-circuit realization of topological corner modes*, Nat. Phys. **14**, 925 (2018), doi:10.1038/s41567-018-0246-1.

[4] Y. Hadad, J. C. Soric, A. B. Khanikaev and A. Alù, *Self-induced topological protection in nonlinear circuit arrays*, Nat. Electron **1**, 178–182 (2018), doi:10.1038/s41928-018-0042-z.

[5] F. Zangeneh-Nejad and R. Fleury, *Nonlinear second-order topological insulators*, Phys. Rev. Lett. **123**, 053902 (2019), doi:10.1103/PhysRevLett.123.053902.

[6] T. Ozawa, H. M. Price, A. Amo, N. Goldman, M. Hafezi, L. Lu, M. C. Rechtsman, D. Schuster, J. Simon, O. Zilberberg and I. Carusotto, *Topological photonics*, Rev. Mod. Phys. **91**, 015006 (2019), doi:10.1103/RevModPhys.91.015006.

[7] A. B. Khanikaev, S. H. Mousavi, W.-K. Tse, M. Kargarian, A. H. MacDonald and G. Shvets, *Photonic topological insulators*, Nat. Mater. **12**, 233–239 (2013), doi:10.1038/nmat3520.

[8] M. Serra-Garcia, V. Peri, R. Süsstrunk, O. R. Bilal, T. Larsen, L. G. Villanueva and S. D. Huber, *Observation of a phononic quadrupole topological insulator*, Nature **555**, 342 (2018), doi:10.1038/nature25156.

[9] G. G. Pyrialakos, N. Schmitt, N. S. Nye, M. Heinrich, N. V. Kantartzis, A. Szameit and D. N. Christodoulides, *Symmetry-controlled edge states in the type-ii phase of dirac photonic lattices*, Nat. Commun. **11**, 2074 (2020), doi:10.1038/s41467-020-15952-z.

[10] D. Smirnova, D. Leykam, Y. Chong and Y. Kivshar, *Nonlinear topological photonics*, Appl. Phys. Rev. **7**(2), 021306 (2020), doi:10.1063/1.5142397.

[11] G. Ma, M. Xiao and C. T. Chan, *Topological phases in acoustic and mechanical systems*, Nat. Rev. Phys. **1**, 281–294 (2019), doi:10.1038/s42254-019-0030-x.

[12] H. Xue, Y. Yang and B. Zhang, *Topological acoustics*, Nat. Rev. Mater. **7**, 974–990 (2022), doi:10.1038/s41578-022-00465-6.

[13] Z. Yang, F. Gao, X. Shi, X. Lin, Z. Gao, Y. Chong and B. Zhang, *Topological acoustics*, Phys. Rev. Lett. **114**, 114301 (2015), doi:10.1103/PhysRevLett.114.114301.

[14] S. D. Huber, *Topological mechanics*, Nat. Phys. **12**, 621 (2016), doi:10.1038/nphys3801.

[15] A. Souslov, B. C. van Zuiden, D. Bartolo and V. Vitelli, *Topological sound in active-liquid metamaterials*, Nat. Phys. **13**, 1091 (2017), doi:10.1038/nphys4193.

[16] C. He, X. Ni, H. Ge, X.-C. Sun, Y.-B. Chen, M.-H. Lu, X.-P. Liu and Y.-F. Chen, *Acoustic topological insulator and robust one-way sound transport*, Nat. Phys. **12**, 1124 (2016), doi:10.1038/nphys3867.

[17] D. Wang, Y. Deng, J. Ji, M. Oudich, W. A. Benalcazar, G. Ma and Y. Jing, *Realization of a - classified chiral-symmetric higher-order topological insulator in a coupling-inverted acoustic crystal*, Phys. Rev. Lett. **123**, 053902 (2019), doi:10.1103/PhysRevLett.123.053902.

[18] H. Xue, Y. Yang, F. Gao, Y. Chong and B. Zhang, *Acoustic higher-order topological insulator on a kagome lattice*, Nat. Mater. **18**, 108–112 (2019), doi:10.1038/s41563-018-0251-x.

[19] F. Zangeneh-Nejad and R. Fleury, *Disorder-induced signal filtering with topological metamaterials*, Adv. Mater. **32**(28), 2001034 (2020), doi:10.1002/adma.202001034.

[20] A. Coutant, A. Sivadon, L. Zheng, V. Achilleos, O. Richoux, G. Theocharis and V. Pagneux, *Acoustic su-schrieffer-heeger lattice: Direct mapping of acoustic waveguides to the su-schrieffer-heeger model*, Phys. Rev. B **103**, 224309 (2021), doi:10.1103/PhysRevB.103.224309.

[21] S. Shankar, A. Souslov, M. J. Bowick, M. C. Marchetti and V. Vitelli, *Topological active matter*, Nat. Rev. Mater. **4**, 380 (2022), doi:10.1038/s42254-022-00445-3.

[22] X. Zhang, F. Zangeneh-Nejad, Z.-G. Chen, M.-H. Lu and J. Christensen, *A second wave of topological phenomena in photonics and acoustics*, Nature **618**, 687–697 (2023), doi:10.1038/s41586-023-06163-9.

[23] D. A. Dobrykh, A. V. Yulin, A. P. Slobozhanyuk, A. N. Poddubny and Y. S. Kivshar, *Nonlinear control of electromagnetic topological edge states*, Phys. Rev. Lett. **121**, 163901 (2018), doi:10.1103/PhysRevLett.121.163901.

[24] Y. Wang, L.-J. Lang, C. H. Lee, B. Zhang and Y. D. Chong, *Topologically enhanced harmonic generation in a nonlinear transmission line metamaterial*, Nat. Commun. **10**, 1102 (2019).

[25] M. Serra-Garcia, R. Süsstrunk and S. D. Huber, *Observation of quadrupole transitions and edge mode topology in an lc circuit network*, Phys. Rev. B **99**, 020304 (2019), doi:10.1103/PhysRevB.99.020304.

[26] L. J. Maczewsky, M. Heinrich, M. Kremer, S. K. Ivanov, M. Ehrhardt, F. Martinez, Y. V. Kartashov, V. V. Konotop, L. Torner, D. Bauer and A. Szameit, *Nonlinearity-induced photonic topological insulator*, Science **370**(6517), 701 (2020), doi:10.1126/science.abd2033.

[27] S. Mukherjee and M. C. Rechtsman, *Observation of floquet solitons in a topological bandgap*, Science **368**(6493), 856 (2020), doi:10.1126/science.aba8725.

[28] Z. Hu, D. Bongiovanni, D. Jukić, E. Jajtić, S. Xia, D. Song, J. Xu, R. Morandotti, H. Buljan and Z. Chen, *Nonlinear control of photonic higher-order topological bound states in the continuum*, Light Sci. Appl. **10**, 164 (2021), doi:10.1038/s41377-021-00607-5.

[29] D. D. Snee and Y.-P. Ma, *Edge solitons in a nonlinear mechanical topological insulator*, Extreme Mech. Lett. **30**, 100487 (2019), doi:10.1016/j.eml.2019.100487.

[30] P.-W. Lo, C. D. Santangelo, B. G.-g. Chen, C.-M. Jian, K. Roychowdhury and M. J. Lawler, *Topology in nonlinear mechanical systems*, Phys. Rev. Lett. **127**, 076802 (2021), doi:10.1103/PhysRevLett.127.076802.

[31] R. Chaunsali and G. Theocharis, *Self-induced topological transition in phononic crystals by nonlinearity management*, Phys. Rev. B **100**, 014302 (2019), doi:10.1103/PhysRevB.100.014302.

[32] A. Darabi and M. J. Leamy, *Tunable nonlinear topological insulator for acoustic waves*, Phys. Rev. Appl. **12**, 044030 (2019), doi:10.1103/PhysRevApplied.12.044030.

[33] R. Chaunsali, H. Xu, J. Yang, P. G. Kevrekidis and G. Theocharis, *Stability of topological edge states under strong nonlinear effects*, Phys. Rev. B **103**, 024106 (2021), doi:10.1103/PhysRevB.103.024106.

[34] S. Xia, D. Kaltsas, D. Song, I. Komis, J. Xu, A. Szameit, H. Buljan, K. G. Makris and Z. Chen, *Nonlinear tuning of pt symmetry and non-hermitian topological states*, Science **372**(6537), 72 (2021), doi:10.1126/science.abf6873.

[35] Y. Hadad, A. B. Khanikaev and A. Alù, *Self-induced topological transitions and edge states supported by nonlinear staggered potentials*, Phys. Rev. B **93**, 155112 (2016), doi:10.1103/PhysRevB.93.155112.

[36] A. Bisianov, M. Wimmer, U. Peschel and O. A. Egorov, *Stability of topologically protected edge states in nonlinear fiber loops*, Phys. Rev. A **100**, 063830 (2019), doi:10.1103/PhysRevA.100.063830.

[37] D. A. Smirnova, L. A. Smirnov, D. Leykam and Y. S. Kivshar, *Topological edge states and gap solitons in the nonlinear dirac model*, Laser Photonics Rev **13**(12), 1900223 (2019), doi:10.1002/lpor.201900223.

[38] T. Tuloup, R. W. Bomantara, C. H. Lee and J. Gong, *Nonlinearity induced topological physics in momentum space and real space*, Phys. Rev. B **102**, 115411 (2020), doi:10.1103/PhysRevB.102.115411.

[39] M. S. Kirsch, Y. Zhang, M. Kremer, L. J. Maczewsky, S. K. Ivanov, Y. V. Kartashov, D. B. Lluis Torner, A. Szameit and M. Heinrich, *Nonlinear second-order photonic topological insulators*, Nat. Phys. **17**, 995 (2021), doi:10.1038/s41567-021-01275-3.

[40] B.-U. Sohn, Y.-X. Huang, J. W. Choi, G. F. R. Chen, D. K. T. Ng, S. A. Yang and D. T. H. Tan, *A topological nonlinear parametric amplifier*, Nat. Commun. **13**, 7218 (2022), doi:10.1038/s41467-022-34979-y.

[41] B. M. Manda, V. Achilleos, O. Richoux, C. Skokos and G. Theocharis, *Wave-packet spreading in the disordered and nonlinear su-schrieffer-heeger chain*, Phys. Rev. B **107**, 184313 (2023), doi:10.1103/PhysRevB.107.184313.

[42] R. Chaunsali, P. G. Kevrekidis, D. Frantzeskakis and G. Theocharis, *Dirac solitons and topological edge states in the β-fermi-pasta-ulam-tsingou dimer lattice*, Phys. Rev. E **108**, 054224 (2023), doi:10.1103/PhysRevE.108.054224.

[43] J. Rogel-Salazar, *The gross–pitaevskii equation and bose–einstein condensates*, Eur. J. Phys. **34**(2), 247 (2013), doi:10.1088/0143-0807/34/2/247.

[44] D. Leykam and Y. D. Chong, *Edge solitons in nonlinear-photonic topological insulators*, Phys. Rev. Lett. **117**, 143901 (2016), doi:10.1103/PhysRevLett.117.143901.

[45] Y. Hadad, V. Vitelli and A. Alu, *Solitons and propagating domain walls in topological resonator arrays*, ACS Photonics **4**(8), 1974 (2017), doi:10.1021/acsphotonics.7b00303.

[46] S. Kruk, A. Poddubny, D. Smirnova, L. Wang, A. Slobozhanyuk, A. Shorokhov, I. Kravchenko, B. Luther-Davies and Y. Kivshar, *Nonlinear light generation in topological nanostructures*, Nat. Nanotechnol **14**, 126 (2019), doi:10.1038/s41565-018-0324-7.

[47] D. Smirnova, S. Kruk, D. Leykam, E. Melik-Gaykazyan, D.-Y. Choi and Y. Kivshar, *Third-harmonic generation in photonic topological metasurfaces*, Phys. Rev. Lett. **123**, 103901 (2019), doi:10.1103/PhysRevLett.123.103901.

[48] Z. Lan, J. W. You and N. C. Panoiu, *Nonlinear one-way edge-mode interactions for frequency mixing in topological photonic crystals*, Phys. Rev. B **101**, 155422 (2020), doi:10.1103/PhysRevB.101.155422.

[49] H. Hohmann, T. Hofmann, T. Helbig, S. Imhof, H. Brand, L. K. Upreti, A. Stegmaier, A. Fritzsche, T. Müller, U. Schwingenschlögl, C. H. Lee, M. Greiter *et al.*, *Observation of cnoidal wave localization in nonlinear topolectric circuits*, Phys. Rev. Res. **5**, L012041 (2023), doi:10.1103/PhysRevResearch.5.L012041.

[50] C.-K. Chiu, J. C. Y. Teo, A. P. Schnyder and S. Ryu, *Classification of topological quantum matter with symmetries*, Rev. Mod. Phys. **88**, 035005 (2016), doi:10.1103/RevModPhys.88.035005.

[51] D. Zhou, D. Z. Rocklin, M. Leamy and Y. Yao, *Topological invariant and anomalous edge modes of strongly nonlinear systems*, Nat. Commun. **13**, 3379 (2022), doi:10.1038/s41467-022-31084-y.

[52] X. Ni, M. Weiner, A. Alù and A. B. Khanikaev, *Observation of higher-order topological acoustic states protected by generalized chiral symmetry*, Nat. Mater. **18**, 113–120 (2019), doi:10.1038/s41563-018-0252-9.

[53] L. Jezequel and P. Delplace, *Nonlinear edge modes from topological one-dimensional lattices*, Phys. Rev. B **105**, 035410 (2022), doi:10.1103/PhysRevB.105.035410.

[54] Z. Wang, X. Wang, Z. Hu, D. Bongiovanni, D. Jukić, L. Tang, D. Song, R. Morandotti, Z. Chen and H. Buljan, *Sub-symmetry-protected topological states*, Nat. Phys. **19**, 992 (2023), doi:10.1038/s41567-023-02011-9.

[55] C. L. Kane and T. C. Lubensky, *Topological boundary modes in isostatic lattices*, Nat. Phys. **10**, 39 (2014), doi:10.1038/nphys2835.

[56] V. Marinca and N. Herisanu, *The method of harmonic balance*, pp. 31–45, Springer Berlin Heidelberg, Berlin, Heidelberg, ISBN 978-3-642-22735-6, doi:10.1007/978-3-642-22735-6 (2011).

[57] X. Guo, V. E. Gusev, K. Bertoldi and V. Tournat, *Manipulating acoustic wave reflection by a nonlinear elastic metasurface*, J. Appl. Phys. **123**(12), 124901 (2018), doi:10.1063/1.5015952.

[58] X. Guo, V. E. Gusev, V. Tournat, B. Deng and K. Bertoldi, *Frequency-doubling effect in acoustic reflection by a nonlinear, architected rotating-square metasurface*, Phys. Rev. E **99**, 052209 (2019), doi:10.1103/PhysRevE.99.052209.

[59] E. Hairer, S. P. Norsett and G. Wanner, *Runge-Kutta and Extrapolation Methods*, pp. 129–353, Springer Berlin Heidelberg, Berlin, Heidelberg, ISBN 978-3-540-78862-1, doi:10.1007/978-3-540-78862-1_2 (1993).

[60] E. Rivet, S. Karkar and H. Lissek, *Broadband low-frequency electroacoustic absorbers through hybrid sensor-/shunt-based impedance control*, IEEE Trans. Control Syst. Technol. **25**(1), 63 (2017), doi:10.1109/TCST.2016.2547981.

[61] X. Guo, H. Lissek and R. Fleury, *Improving sound absorption through nonlinear active electroacoustic resonators*, Phys. Rev. Appl. **13**, 014018 (2020), doi:10.1103/PhysRevApplied.13.014018.

[62] X. Guo, H. Lissek and R. Fleury, *Observation of non-reciprocal harmonic conversion in real sounds*, Commun. Physics. **6**, 93 (2023), doi:10.1038/s42005-023-01217-w.

[63] M. Padlewski, M. Volery, R. Fleury, H. Lissek and X. Guo, *Active acoustic su-schrieffer-heeger-like metamaterial*, Phys. Rev. Appl. **20**, 014022 (2023), doi:10.1103/PhysRevApplied.20.014022.